FE^2 multi-scale framework for the two-equation model of transient heat conduction in two-phase media

Zhuo, Mingzhao

Important note
To cite this publication, please use the final published version (if applicable).
Please check the document version above.

FE² multi-scale framework for the two-equation model of transient heat conduction in two-phase media

Mingzhao Zhuo [a,b,*]

[a] *Faculty of Civil Engineering and Geosciences, Delft University of Technology, Delft, The Netherlands*
[b] *Department of Mechanical Engineering, Imperial College London, London, United Kingdom*

ABSTRACT

In the study of transient heat conduction in heterogeneous two-phase media, the local thermal non-equilibrium condition calls for the use of a two-equation model to appropriately describe different temperatures in the two phases. We propose for the two-equation model an FE² multi-scale framework that is capable of addressing nonlinear conduction problems. The FE² framework consists of volume-averaged macroscale equations, well-defined microscale problems, and the information exchange between the two scales. Compared to a traditional FE² method for the one-equation model, the proposed FE² framework introduces an additional source term at the macroscale that is upscaled from the microscale interfacial heat transfer. At variance with the tangent matrices (i.e., effective conductivity) of the heat flux, the tangent matrices of the interfacial heat transfer depend on the microscopic length scale. The proposed FE² framework is validated against single-scale direct numerical simulations, and some numerical examples are employed to demonstrate its potential.

1. Introduction

The need for a two-equation model to describe the transient heat conduction process in a two-phase medium has long been recognized, especially when the local equilibrium condition breaks down [1–8]. Although computationally efficient, the conventional volume averaging method [9–11] is often limited to linear problems due to the complexity in solving the closure problems for effective transport properties and the interfacial heat transfer coefficient. Here we propose an FE² multi-scale framework that allows for nonlinear transport for the two-equation model of transient heat conduction in a two-phase medium.

Transient transport phenomena in heterogeneous materials have been traditionally addressed with the one-equation model, in which only one macroscale variable is defined on a homogenized volume originally consisting of multiple phases (for simplicity, we restrict the study to a two-phase medium). The one-equation model is suited to the local equilibrium assumption—averaged temperatures of the two phases are close or even the same—that usually holds when their transport properties are sufficiently close and the microscopic length scale is adequately small

for fast heat transfer. However, when these conditions do not hold and there is net heat transfer from one phase to the other, the local equilibrium will break down. One such case is when there is a significant heat generation in any of the two phases (as discussed in Section 5.1.1, Kuwahara et al. [3], and Kaviany [12]) or, analogously, a kinetic reaction source in the biofilm phase in porous media in environmental engineering applications [5,6]. Another scenario leading to equilibrium breakdown is when there is a great disparity of conductivity between the two phases (as discussed in Section 5.1.2 and Mahmoudi and Karimi [13]). A more general description is required for the separate treatment of average values in the two phases and the explicit description of the interfacial heat transfer [1,3,7,8,14,15]. This general strategy is termed the two-equation model, according to the work by Quintard et al. [1,2].

The two-equation model is also required when the two phases are characterized by different physics. By way of example, in lithium-ion battery cells [16,17], electrodes consist of active materials, electrolyte, and conductive materials. During the (dis)charging process, lithium ions diffuse and migrate in the electrolyte, while lithium diffuses in the active material. The quantities of concern in the two phases, the concentration of lithium ions in the electrolyte and concentration of lithium in the active material, differ in the physical meaning and thus need to be considered as two different field variables, and their values are generally not equal [16,17].

* Corresponding author.
E-mail addresses: m.zhuo@tudelft.nl, mzhuo@connect.ust.hk

They are connected through the consistence of mass flux between the two phases ensured by chemical reactions occurring on the interface, described for example by the Butler-Volmer equation [16].

Traditionally, the two-equation model is solved analytically. Homogenized diffusion equations are first derived at the macroscale via the volume averaging method [11,18]. The so-called closure problems are then defined on the averaging volume at the microscale and solved for the effective transport coefficients and interfacial heat transfer coefficient needed in the homogenized equations [1,9,19]. Despite of computational efficiency, this method is restricted to linear conduction problems and impaired by accuracy concerns due to many simplification assumptions.

Alternatively, an accurate and straightforward method is to perform a single-scale numerical simulation (also called direct numerical simulation in some fields; see Section 2.2). A single-scale simulation resolves the microscopic geometry and therefore is quite accurate; the price for accuracy is the computational cost that could be as high as rendering the simulation infeasible especially when the problem domain spans spatial scales of several orders of magnitude. To avoid the significant simulation cost attached to a fully resolved domain and retain the same level of accuracy, a multi-scale computational technique, called the FE^2 method, has been developed and successfully employed in applications ranging from mechanical equilibrium problems [20–26] to transport problems [27–35].

A brief review on the FE^2 method applied in transient diffusion problems is given as follows. In the seminal works by Özdemir et al. [27,28], a transient heat conduction was considered at the macroscale while a steady-state diffusion was used at the microscale, without any heat sources. The transient effect at the microscale and heat source terms were then considered by Larsson et al. [29], followed by the extension to non-uniform heat sources by Ramos et al. [31]. The model developed in Ramos et al. [31] was also applied to an engineering problem of filled elastomers [32]. To reduce the increased simulation cost caused by considering the microscale transient effect, Aggestam et al. [36] and Waseem et al. [33–35] developed model order reduction techniques within the FE^2 framework.

These existing works however only apply to the one-equation model as they consider one homogenized variable defined on the representative volume element (RVE) and use the effective material properties (stiffness, conductivity) of the whole RVE that may consist of multiple phases. These frameworks cannot offer separate information for each phase (refer to Section 3.5), as needed in applications requiring a two-equation model. The aim of this study is to propose an FE^2 multi-scale framework for the two-equation model. We first employ the volume averaging method to derive the macroscale transient equations (Section 3.1), thus clearly demonstrating the physical meanings of the macroscale field variables and other quantities. All the key ingredients of the FE^2 approach including two-way information flow and microscale problem boundary conditions are then detailed in the remainder of Section 3, followed by its numerical implementation in Section 4. The two-scale framework is validated against single-scale direct numerical simulations through simple academic examples (Section 5.1).

2. Preliminaries

2.1. Volume average operator

With reference to a quantity x_α (a scalar or vector) in the α phase of a two-phase RVE (Fig. 1b), we define the volume average operator with respect to the whole RVE as

$$\langle x_\alpha \rangle = \frac{1}{V} \int_{V_\alpha} x_\alpha \, \mathrm{d}V \tag{1}$$

and the intrinsic volume average [9] over the α phase as

$$\overline{x}_\alpha = \frac{1}{V_\alpha} \int_{V_\alpha} x_\alpha \, \mathrm{d}V, \tag{2}$$

where V denotes the total volume of the two-phase medium, and V_α is the volume of the α phase. The variable α represents either β or σ. If the volume fraction of the α phase is defined as

$$\epsilon_\alpha = \frac{V_\alpha}{V},$$

the following relation between the two volume averages holds:

$$\langle x_\alpha \rangle = \epsilon_\alpha \overline{x}_\alpha. \tag{3}$$

2.2. Single-scale description

The composite under consideration consists of two phases—the matrix (β phase) and the inclusion (σ phase)—as shown in Fig. 1a. The two phases possess different transport properties. Physical quantities associated with β phase and σ phase are distinguished by the subscripts β and σ, respectively. Transient heat conduction in the two-phase medium is governed by

$$c_\beta \frac{\partial u_\beta}{\partial t} + \boldsymbol{\nabla} \cdot \mathbf{h}_\beta = r_\beta \quad \text{in} \quad V_\beta \times (0, t_{\text{end}}] \quad \text{and} \tag{4a}$$

$$c_\sigma \frac{\partial u_\sigma}{\partial t} + \boldsymbol{\nabla} \cdot \mathbf{h}_\sigma = r_\sigma \quad \text{in} \quad V_\sigma \times (0, t_{\text{end}}], \tag{4b}$$

where c, u, $\mathbf{h}$, and r represent, respectively, volumetric heat capacity, temperature, heat flux, and the given volumetric heat source. The heat flux is described by Fourier's law and expressed as

$$\mathbf{h}_\beta = -k_\beta \left(u_\beta \right) \boldsymbol{\nabla} u_\beta, \tag{5a}$$

$$\mathbf{h}_\sigma = -k_\sigma (u_\sigma) \boldsymbol{\nabla} u_\sigma, \tag{5b}$$

where the thermal conductivity for each phase is generally temperature dependent.

Across the interface between the two phases, we consider the temperature continuity condition (i.e., $u_\beta = u_\sigma$). These two governing equations can be readily solved by a standard finite element program. Specifically, each phase will be discretized to form conforming mesh at the interface and a common node will be used. This solution strategy is referred to as the single-scale approach, and it will be used as a reference for the proposed multi-scale approach.

3. Multi-scale framework

This section outlines the FE^2 computational framework where the governing equations at the two scales and the corresponding information-passing procedures are described. The two-scale framework relies on the underlying principle of scale separation [9,37], which states that, referring to Fig. 1a, the characteristic length (l_c) of the inclusions (e.g., radius), the size of the RVE (l_{rve}), and the characteristic length of the macroscale domain (L_c) should satisfy the constraint $l_c \ll l_{\text{rve}} \ll L_c$.

In the remainder of the paper, we use lower case letters to represent microscale quantities while upper case letters refer to macroscale quantities. For example, the microscale temperature is denoted by u, while U represents the macroscale temperature.

3.1. Macroscale problem

The macroscale governing equations are derived by volume-averaging the single-scale formulation presented in the previous
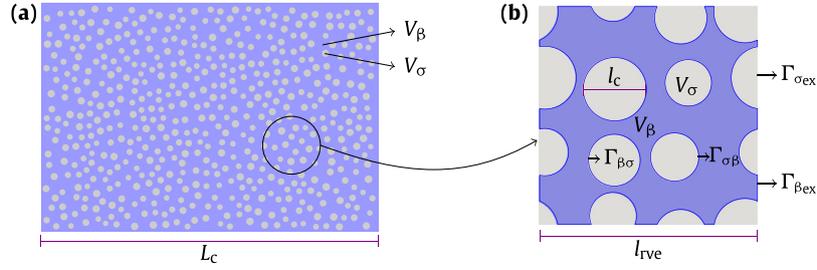
Fig. 1. (a) A two-phase medium consisting of the blue matrix (β phase occupying V_β) and gray inclusions (σ phase occupying V_σ) possessing different transport properties. (b) Microscopic representative volume element (RVE). The RVE boundary Γ_{ex} is divided into two parts, each associated with a phase, such that $\Gamma_{ex} = \Gamma_{\beta_{ex}} \cup \Gamma_{\sigma_{ex}}$ with $\Gamma_{\beta_{ex}} \cap \Gamma_{\sigma_{ex}} = \Phi$. The interface between the two phases is represented by two coinciding boundaries $\Gamma_{\beta\sigma}$ and $\Gamma_{\sigma\beta}$ belonging to the β and σ phases, respectively. L_c, l_{rve}, and l_c characterize the typical length scales of the macroscopic domain, the RVE, and the microscopic constitute phase.

section over an RVE. With reference to the RVE (Fig. 1b), applying the volume average operator (1) to Eq. (4a) yields

$$c_\beta \frac{\partial \langle u_\beta \rangle}{\partial t} + \langle \boldsymbol{\nabla} \cdot \mathbf{h}_\beta \rangle = \langle r_\beta \rangle \quad \text{in} \quad V_\beta \times (0, t_{end}]. \tag{6}$$

The volume-averaged temperature $\langle u_\beta \rangle$ is expressed in terms of the intrinsic average $\overline{u}_\beta$ which is defined as the macroscale temperature U_β:

$$\langle u_\beta \rangle = \epsilon_\beta \overline{u}_\beta = \epsilon_\beta U_\beta, \tag{7}$$

where ϵ_β is the volume fraction of the β phase. The volume-averaged flux divergence is split into two surface integrals (Fig. 1b):

$$\langle \boldsymbol{\nabla} \cdot \mathbf{h}_\beta \rangle = \frac{1}{V} \int_{V_\beta} \boldsymbol{\nabla} \cdot \mathbf{h}_\beta \, dV = \frac{1}{V} \int_{\Gamma_{\beta_{ex}}} \mathbf{h}_\beta \cdot \mathbf{n}_{\beta_{ex}} \, d\Gamma$$
$$+ \frac{1}{V} \int_{\Gamma_{\beta\sigma}} \mathbf{h}_\beta \cdot \mathbf{n}_{\beta\sigma} \, d\Gamma, \tag{8}$$

where $\Gamma_{\beta_{ex}}$ and $\Gamma_{\beta\sigma}$ represent the RVE boundary contributed by the β phase and the interface with the σ phase, respectively, $\mathbf{n}_{\beta_{ex}}$ is the outward-pointing unit vector normal to $\Gamma_{\beta_{ex}}$, and $\mathbf{n}_{\beta\sigma}$ is the unit vector normal to $\Gamma_{\beta\sigma}$ pointing from the β phase to the σ phase. The volume-averaged heat source in the right-hand side of Eq. (6) is defined as the macroscale heat source

$$R_\beta = \langle r_\beta \rangle, \tag{9}$$

where the volumetric heat source r_β is a given quantity.

Substituting Eq. (7) to (9) into Eq. (6) yields

$$c_\beta \epsilon_\beta \frac{\partial U_\beta}{\partial t} + \frac{1}{V} \int_{\Gamma_{\beta_{ex}}} \mathbf{h}_\beta \cdot \mathbf{n}_{\beta_{ex}} \, d\Gamma = R_\beta - \frac{1}{V} \int_{\Gamma_{\beta\sigma}} \mathbf{h}_\beta \cdot \mathbf{n}_{\beta\sigma} \, d\Gamma. \tag{10}$$

The volume-averaged outflow of heat through the RVE boundary $\Gamma_{\beta_{ex}}$ can be regarded as the divergence of the heat flux at a macroscale point:

$$\frac{1}{V} \int_{\Gamma_{\beta_{ex}}} \mathbf{h}_\beta \cdot \mathbf{n}_{\beta_{ex}} \, d\Gamma = \boldsymbol{\nabla} \cdot \mathbf{H}_\beta, \tag{11}$$

and the heat transfer from the β phase to the σ phase can be defined as the heat sink, or negative heat source, at a macroscale point:

$$\frac{1}{V} \int_{\Gamma_{\beta\sigma}} \mathbf{h}_\beta \cdot \mathbf{n}_{\beta\sigma} \, d\Gamma = -Q_\beta. \tag{12}$$

Macroscale equation (10) can thus be expressed as

$$c_\beta \epsilon_\beta \frac{\partial U_\beta}{\partial t} + \boldsymbol{\nabla} \cdot \mathbf{H}_\beta = R_\beta + Q_\beta \quad \text{in} \quad \Omega \times (0, t_{end}], \tag{13a}$$

where Ω denotes the homogenized domain shared by both phases at the macroscale as shown in Fig. 2a. Likewise, we can derive the macroscale equation for the σ phase as

$$c_\sigma \epsilon_\sigma \frac{\partial U_\sigma}{\partial t} + \boldsymbol{\nabla} \cdot \mathbf{H}_\sigma = R_\sigma + Q_\sigma \quad \text{in} \quad \Omega \times (0, t_{end}], \tag{13b}$$

where the macroscale temperature

$$U_\sigma = \overline{u}_\sigma = \frac{\langle u_\sigma \rangle}{\epsilon_\sigma} \tag{14}$$

represents the intrinsic average of the temperature of the σ phase, the macroscale heat source

$$R_\sigma = \langle r_\sigma \rangle \tag{15}$$

is the volume average of the given heat source r_σ, and the additional macroscale heat source

$$Q_\sigma = -\frac{1}{V} \int_{\Gamma_{\sigma\beta}} \mathbf{h}_\sigma \cdot \mathbf{n}_{\sigma\beta} \, d\Gamma \tag{16}$$

is caused by the interfacial heat transfer.

The macroscale heat fluxes ($\mathbf{H}_\beta$ and $\mathbf{H}_\sigma$) and the macroscale heat sources (Q_β and Q_σ) due to interfacial heat transfer in the macroscale governing equation (13) are obtained through the microscale computation. As schematically shown in Fig. 2, the macroscale solution U_β and U_σ and their gradients at an integration point are downscaled to define the microscale problem; the macroscale heat fluxes and sources as well as their tangents are then computed from the microscale solution and upscaled. Moreover, in the microscale simulation the temperature continuity condition ($u_\beta = u_\sigma$) and flux continuity, suggesting $Q_\beta + Q_\sigma = 0$, are simultaneously enforced across the interface.

3.2. Downscaling

The boundary conditions enforced at the microscale level are obtained by downscaling macroscale quantities at each integration point of the macroscale mesh: temperature U_β and U_σ, and their gradients $\boldsymbol{\nabla} U_\beta$ and $\boldsymbol{\nabla} U_\sigma$, respectively. For conciseness, these quantities are stored in a column vector as

$$\mathbf{X} = \left[(\boldsymbol{\nabla} U_\beta)^T \quad U_\beta \quad (\boldsymbol{\nabla} U_\sigma)^T \quad U_\sigma \right]^T. \tag{17}$$

3.3. Microscale problem

The microscale problem is defined on an RVE (Fig. 2b) associated with a macroscale integration point. At variance with the single-scale description (4), the governing equations at the microscale neglect the time evolution terms and consider the steady-state thermal equilibrium [27,29], in view of the relatively small RVE size. The governing equations are thus expressed as

$$\boldsymbol{\nabla} \cdot \mathbf{h}_\beta = b_\beta \quad \text{in} \quad V_\beta \quad \text{and} \tag{18a}$$

$$\boldsymbol{\nabla} \cdot \mathbf{h}_\sigma = b_\sigma \quad \text{in} \quad V_\sigma, \tag{18b}$$

where the constitutive relations for heat fluxes $\mathbf{h}_\beta$ and $\mathbf{h}_\sigma$ are the same as in Eq. (5). The two source terms b_β and b_σ are different

(a) homogenized domain   **(b)**   RVE
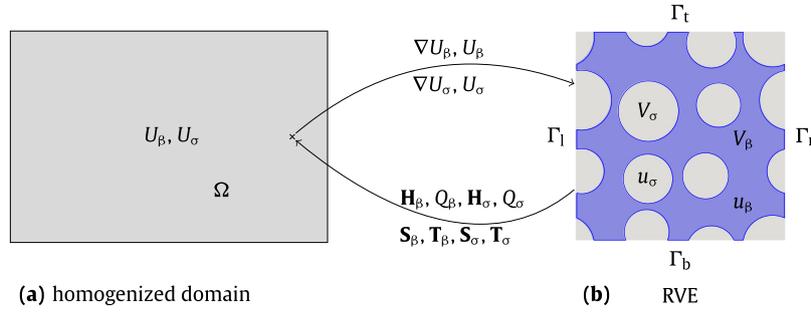
Fig. 2. Homogenized domain at the macroscale, RVE at the microscale, and information exchange between macro- and micro-scales. Macroscale temperatures U_β and U_σ, and their gradients ∇U_β and ∇U_σ are downscaled as boundary conditions for the microscale RVE problem. The homogenized fluxes $\mathbf{H}_\beta$ and $\mathbf{H}_\sigma$ (Eq. (33)), volumetric interfacial heat transfer Q_β (Eq. (12)) and Q_σ (Eq. (16)), and their dependencies $\mathbf{S}_\beta$, $\mathbf{S}_\sigma$, $\mathbf{T}_\beta$, and $\mathbf{T}_\sigma$ (Eq. (34)) on the macroscale quantities $\mathbf{X}$ (Eq. (17)) are then transferred back to the macroscale problem. Panel (b) shows also the boundaries used for the enforcement of periodic boundary conditions in the FE analysis of the RVE: left (Γ_l) and bottom (Γ_b) edges are categorized into the master boundary $\Gamma_{lb} = \Gamma_l \cup \Gamma_b$, while the right ($\Gamma_r$) and top ($\Gamma_t$) edges (corresponding to Γ_l and Γ_b, respectively) are considered as parts of the slave boundary $\Gamma_{rt} = \Gamma_r \cup \Gamma_t$.

from the given source terms r_β and r_σ in the single-scale equation (4). The prescribed heat sources (r_β and r_σ) are included in the macroscale governing equation (13) in an average sense—R_β in Eq. (9) and R_σ in Eq. (15)—and will be indirectly reflected at the microscale through the enforcement of consistent temperatures across the two scales as expressed by Eq. (26). The two terms b_β and b_σ actually reflect unknown heat sources caused by enforcing the constraint (26), acting as constraint forces and regardless of the given heat sources r_β and r_σ.

Next, the microscale boundary conditions are derived from the macroscale quantities $\mathbf{X}$ (Eq. (17)). By convention in the FE^2 analysis, the microscale temperature profiles $u_\beta(\mathbf{x})$ and $u_\sigma(\mathbf{x})$, with $\mathbf{x}$ as the position vector, can be decomposed into a spatially linear field (first two terms) and a fluctuation filed (the last term):

$$u_\beta = U_\beta + \boldsymbol{\nabla} U_\beta \cdot (\mathbf{x} - \mathbf{x}_{ra}) + \tilde{u}_\beta, \tag{19a}$$

$$u_\sigma = U_\sigma + \boldsymbol{\nabla} U_\sigma \cdot (\mathbf{x} - \mathbf{x}_{rb}) + \tilde{u}_\sigma, \tag{19b}$$

where $\mathbf{x}_{ra}$ and $\mathbf{x}_{rb}$ are reference points.

In the FE^2 analyses of mechanical problems [23,37], it is a common practice to assume that the macroscale deformation gradient at a point is equal to the volume average of the microscale counterpart over the whole RVE defined on that point. This assumption, connecting the macro- and micro-scales, is known as the averaging theorem [38]. Likewise, in the FE^2 analysis of heat conduction [27], the macroscale temperature gradient is usually assumed to be equal to the volume average of the microscale temperature gradient. This assumption results from the simplest and widely-used first-order homogenization; the macroscale temperature gradient is used as a loading for the microscale problem [29] through the boundary conditions imposed on the RVE.

The transfer of temperature gradient for the one-equation model [27] is as straightforward as the strain transfer. However, it requires special consideration in the two-equation model since there are two macroscale temperature gradients—$\boldsymbol{\nabla} U_\beta$ and $\boldsymbol{\nabla} U_\sigma$. Here we propose the following relations as an equivalent for the assumption described above:

$$\frac{1}{V} \int_{\Gamma_{ex}} u_\beta \mathbf{n}_{ex}\, d\Gamma = \boldsymbol{\nabla} U_\beta, \tag{20a}$$

$$\frac{1}{V} \int_{\Gamma_{ex}} u_\sigma \mathbf{n}_{ex}\, d\Gamma = \boldsymbol{\nabla} U_\sigma, \tag{20b}$$

where $\mathbf{n}_{ex}$ is the outward-pointing normal vector to the RVE boundary Γ_{ex} and the surface integral is over the whole RVE bound-

ary $\Gamma_{ex} = \Gamma_{\beta ex} \cup \Gamma_{\sigma ex}$ (Fig. 1b). The surface integral is equivalent to the previously mentioned volume integral via the divergence theorem but is preferred especially when holes/voids exist in the RVE [24,39,40]. Here, the σ phase regions act as holes for the β phase, and vice versa.

Substituting Eq. (19a) into Eq. (20a) results in

$$\frac{1}{V} \int_{\Gamma_{ex}} u_\beta \mathbf{n}_{ex}\, d\Gamma = \boldsymbol{\nabla} U_\beta + \frac{1}{V} \int_{\Gamma_{ex}} \tilde{u}_\beta \mathbf{n}_{ex}\, d\Gamma. \tag{21}$$

In the derivation, $\mathbf{n}_{ex}$ should be evaluated at every point on the whole RVE boundary including the portion for the σ phase ($\Gamma_{\sigma ex}$) although u_β is only defined in the β phase. This procedure is necessary because the σ phase is the complementary voids of the β phase in the RVE. To the void phase σ we can attach fictitious u_β values and null conductivity, analogous to null stiffness in mechanical problems [24,40]. Comparison of Eq. (21) with Eq. (20a) yields

$$\int_{\Gamma_{ex}} \tilde{u}_\beta \mathbf{n}_{ex}\, d\Gamma = 0, \tag{22a}$$

Similarly, for the σ phase we arrive at

$$\int_{\Gamma_{ex}} \tilde{u}_\sigma \mathbf{n}_{ex}\, d\Gamma = 0. \tag{22b}$$

Constraints (22) are enforced by means of periodic boundary conditions [23,24,41] as "periodic boundary conditions have been proven to be most versatile" [37], not only for periodic but also for arbitrary microstructures [42]. For the two-phase composition of the RVE boundary in Fig. 2b, the periodic boundary conditions are stated as

$$\tilde{u}_\beta(\mathbf{x}_{lb}) = \tilde{u}_\beta(\mathbf{x}_{rt}), \tag{23a}$$

$$\tilde{u}_\sigma(\mathbf{x}_{lb}) = \tilde{u}_\sigma(\mathbf{x}_{rt}), \tag{23b}$$

where $\mathbf{x}_{lb}$ represents an arbitrary point on the left and bottom boundaries and its counterpart on the right and top boundaries is denoted as $\mathbf{x}_{rt}$. Substituting Eq. (23) into Eq. (19) leads to

$$u_\beta(\mathbf{x}_{lb}) - u_\beta(\mathbf{x}_{rt}) - \boldsymbol{\nabla} U_\beta \cdot (\mathbf{x}_{lb} - \mathbf{x}_{rt}) = 0, \tag{24a}$$

$$u_\sigma(\mathbf{x}_{lb}) - u_\sigma(\mathbf{x}_{rt}) - \boldsymbol{\nabla} U_\sigma \cdot (\mathbf{x}_{lb} - \mathbf{x}_{rt}) = 0. \tag{24b}$$

The temperature continuity condition at the two-phase interface is also enforced and expressed as

$$\left[u_\beta \right]_{\Gamma_{\beta\sigma}} - \left[u_\sigma \right]_{\Gamma_{\sigma\beta}} = 0. \tag{25}$$

Moreover, from the definition of the macroscale temperatures in Eq. (7) and (14), we have two additional constraints:

$$\overline{u}_\beta - U_\beta = 0, \tag{26a}$$

$$\overline{u}_\sigma - U_\sigma = 0. \tag{26b}$$

These two extra constraints are necessary for the solution of the microscale problem as they 1) allow us to objectively determine unique microscale solutions for each phase (the reference points in Eq. (19) are not determined), and 2) enforce the consistency of the stored heat in each phase between the macro- and micro-scales. The latter aspect is fundamental: enforcing the heat consistency constraint indirectly applies the heat source to the microscale governing equation (18), which is only explicitly implemented in the macroscale equation (13).

3.4. Upscaling

To close the information exchange loop, the homogenized fluxes $\mathbf{H}_\beta$ and $\mathbf{H}_\sigma$ and their tangent matrices are calculated from the microscale solution and upscaled to the macroscale computation (Fig. 2). The homogenized fluxes are pragmatically calculated as the volume averages of the corresponding microscale heat fluxes [38]:

$$\mathbf{H}_\beta = \frac{1}{V} \int_{V_\beta} \mathbf{h}_\beta \, dV, \tag{27a}$$

$$\mathbf{H}_\sigma = \frac{1}{V} \int_{V_\beta} \mathbf{h}_\sigma \, dV. \tag{27b}$$

For the sake of numerical implementation, the volume integrals are often transformed into surface integrals. The right-hand side of Eq. (27a) is reformulated as

$$\frac{1}{V} \int_{V_\beta} \mathbf{h}_\beta \, dV = \frac{1}{V} \int_{V_\beta} \left[\boldsymbol{\nabla} \cdot \left(\mathbf{x}\, \mathbf{h}_\beta \right) - \mathbf{x} \boldsymbol{\nabla} \cdot \mathbf{h}_\beta \right] dV$$

$$= \frac{1}{V} \int_{\Gamma_{\beta_{ex}}} \mathbf{x}\, \mathbf{h}_\beta \cdot \mathbf{n}_{\beta_{ex}} \, d\Gamma + \left(\frac{1}{V} \int_{\Gamma_{\beta\sigma}} \mathbf{x}\, \mathbf{h}_\beta \cdot \mathbf{n}_{\beta\sigma} \, d\Gamma - \frac{1}{V} \int_{V_\beta} \mathbf{x}\, b_\beta \, dV \right), \tag{28}$$

where the divergence theorem and the microscale governing equation (18a) are used in the derivation. The last two terms in the bracket of Eq. (28) approximate to each other and can be neglected. The demonstration is as follows. Applying volume integral to Eq. (18a) yields

$$\frac{1}{V} \int_{V_\beta} \left(\boldsymbol{\nabla} \cdot \mathbf{h}_\beta - b_\beta \right) dV = 0$$

$$= \frac{1}{V} \int_{\Gamma_{\beta_{ex}}} \mathbf{h}_\beta \cdot \mathbf{n}_{\beta_{ex}} \, d\Gamma + \frac{1}{V} \int_{\Gamma_{\beta\sigma}} \mathbf{h}_\beta \cdot \mathbf{n}_{\beta\sigma} \, d\Gamma - \frac{1}{V} \int_{V_\beta} b_\beta \, dV. \tag{29}$$

The first term in the right-hand side of Eq. (29) actually vanishes. According to the periodic boundary condition (24a), we evaluate $\mathbf{h}_\beta \cdot \mathbf{n}_{\beta_{ex}}$ at the master boundary Γ_{lb} (left and bottom edges) to be the opposite of that at the corresponding slave boundary Γ_{rt} (right and top edges). This is called the anti-periodic normal flux boundary condition [27] and its enforcement through Lagrange multipliers is detailed in Section 4.2. Therefore, the last two terms in Eq. (29) should cancel out each other. Multiplying them by a position vector gives

$$\frac{1}{V} \int_{\Gamma_{\beta\sigma}} \mathbf{x}_c \, \mathbf{h}_\beta \cdot \mathbf{n}_{\beta\sigma} \, d\Gamma = \frac{1}{V} \int_{V_\beta} \mathbf{x}_c \, b_\beta \, dV, \tag{30}$$

where $\mathbf{x}_c$ denotes the geometry center of the RVE. The unknown heat source b_β due to the constraint (26a) is uniform in the RVE domain because a single Lagrange multiplier is used to impose the constraint (26a). Therefore, the right-hand term in Eq. (30) is equal to the last term in Eq. (28)

$$\frac{1}{V} \int_{V_\beta} \mathbf{x}_c \, b_\beta \, dV = \frac{1}{V} \int_{V_\beta} \mathbf{x}\, b_\beta \, dV. \tag{31}$$

In view of Eqs. (30) and (31), the subtraction in the bracket of Eq. (28) is calculated as

$$\frac{1}{V} \int_{\Gamma_{\beta\sigma}} \mathbf{x}\, \mathbf{h}_\beta \cdot \mathbf{n}_{\beta\sigma} \, d\Gamma - \frac{1}{V} \int_{V_\beta} \mathbf{x}\, b_\beta \, dV$$

$$= \frac{1}{V} \int_{\Gamma_{\beta\sigma}} (\mathbf{x} - \mathbf{x}_c) \, \mathbf{h}_\beta \cdot \mathbf{n}_{\beta\sigma} \, d\Gamma. \tag{32}$$

Due to the relatively small RVE size, the right-hand term in Eq. (32) can be assumed to be null and thus ignored, which has also been numerically validated in our simulations. The above derivations also apply to the σ phase, and hence the macroscale heat fluxes in Eq. (27) can be expressed in terms of surface integrals as

$$\mathbf{H}_\beta = \frac{1}{V} \int_{\Gamma_{\beta_{ex}}} \mathbf{x}\, \mathbf{h}_\beta \cdot \mathbf{n}_{\beta_{ex}} \, d\Gamma, \tag{33a}$$

$$\mathbf{H}_\sigma = \frac{1}{V} \int_{\Gamma_{\sigma_{ex}}} \mathbf{x}\, \mathbf{h}_\sigma \cdot \mathbf{n}_{\sigma_{ex}} \, d\Gamma. \tag{33b}$$

The volumetric interfacial heat transfer Q_β and Q_σ are calculated according to Eqs. (12) and (16). Moreover, the dependencies

$$\mathbf{S}_\beta = \frac{\partial \mathbf{H}_\beta}{\partial \mathbf{X}}, \quad \mathbf{T}_\beta = \frac{\partial Q_\beta}{\partial \mathbf{X}}, \tag{34a}$$

$$\mathbf{S}_\sigma = \frac{\partial \mathbf{H}_\sigma}{\partial \mathbf{X}}, \quad \mathbf{T}_\sigma = \frac{\partial Q_\sigma}{\partial \mathbf{X}} \tag{34b}$$

of these quantities with respect to the macroscale quantities $\mathbf{X}$ (Eq. (17)) are also passed back to the macroscale.

The upscaled tangent matrices in Eq. (34) express general dependences on all the downscale macroscale quantities, as $\mathbf{X}$ includes both U_β and U_σ as well as their gradients. This feature is especially important to multi-physics problems where highly-coupled constitutive relations are used at the microscale. The FE^2 downscaling-upscaling procedure thus serves to numerically upscale the general nonlinear constitutive relation at the microscale to the macroscale.

3.5. Comparison with one-equation model

The obvious similarity between the structures of the one- and two-equation models calls for a simple comparison. Adding Eqs. (13a) and (13b) together results in

$$c \frac{\partial U}{\partial t} + \boldsymbol{\nabla} \cdot \mathbf{H} = R_\beta + R_\sigma, \tag{35}$$

where the volumetric heat capacity

$$c = c_\beta \epsilon_\beta + c_\sigma \epsilon_\sigma \tag{36}$$

represents the volume-averaged heat capacity, the homogenized temperature is the total thermal energy over the volume-averaged heat capacity

$$U = \frac{c_\beta \epsilon_\beta U_\beta + c_\sigma \epsilon_\sigma U_\sigma}{c}, \tag{37}$$

and the macroscale heat flux $\mathbf{H}$ is equal to

$$\mathbf{H} = \mathbf{H}_\beta + \mathbf{H}_\sigma. \tag{38}$$

Comparing the preceding equations with those in the one-equation model in Özdemir et al. [27], it can be seen that the volume-averaged heat capacity c and the macroscale heat flux $\mathbf{H}$ (substituting Eq. (27) into Eq. (38)) have the same meanings as

defined in Özdemir et al. [27]. The macroscale temperature in Özdemir et al. [27] is not defined with an explicit meaning, but from this comparison we know it has exactly the same meaning as U in Eq. (37), i.e., the total thermal energy over the volume-averaged heat capacity, but not the volume-averaged temperature

$$U = \epsilon_\beta U_\beta + \epsilon_\sigma U_\sigma. \tag{39}$$

However, if the heat capacities of the two phases are the same ($c_\beta = c_\sigma$), the macroscale temperature (Eq. (37)) of the one-equation model reduces to the volume-averaged temperature.

Because of the equivalence, the one-equation model can be considered as a special case of the two-equation model.

4. Implementation of the multi-scale framework

This section provides the numerical implementation of the FE^2 framework: the finite element procedures for the macroscale and microscale problems and the numerical scheme for the calculation of the upscaled quantities. We condense the standard finite element procedures (readers are referred to textbooks [43,44] for more details) while elaborate the necessary steps specific to the FE^2 method, i.e., the boundary setting of microscale problem and extraction of homogenized quantities. Note that all vectors are column vectors by default.

4.1. Finite element method for macroscale problem

According to standard finite element procedures, the weak form of the macroscale governing equation (13) is expressed as

$$\int_\Omega c_\beta \epsilon_\beta \frac{\partial U_\beta}{\partial t} \delta U_\beta \, dV - \int_\Omega \boldsymbol{\nabla} \delta U_\beta \cdot \mathbf{H}_\beta \, dV - \int_\Omega \left(Q_\beta + R_\beta\right) \delta U_\beta \, dV$$
$$+ \int_{\partial\Omega} \overline{H}_\beta \delta U_\beta \, d\Gamma = 0, \tag{40a}$$

$$\int_\Omega c_\sigma \epsilon_\sigma \frac{\partial U_\sigma}{\partial t} \delta U_\sigma \, dV - \int_\Omega \boldsymbol{\nabla} \delta U_\sigma \cdot \mathbf{H}_\sigma \, dV - \int_\Omega (Q_\sigma + R_\sigma) \, \delta U_\sigma \, dV$$
$$+ \int_{\partial\Omega} \overline{H}_\sigma \delta U_\sigma \, d\Gamma = 0, \tag{40b}$$

where δU_β and δU_σ are variations of field variables, $\overline{H}_\beta$ and $\overline{H}_\sigma$ are prescribed heat fluxes at the macroscale boundaries $\partial\Omega$, and R_β and R_σ are calculated from given microscale heat sources via Eqs. (9) and (15).

The macroscale heat fluxes $\mathbf{H}_\beta$ and $\mathbf{H}_\sigma$ and the heat sources Q_β and Q_σ due to interfacial heat transfer at an integration point are calculated from the microscale problem solution and generally depend on temperatures U_β and U_σ. Because of the coupling of the two governing equations, they are solved simultaneously; therefore, each node in the spatial discretization has two degrees of freedom, one for U_β and the other for U_σ.

A standard finite element approximation is used to discretize the field variables in the spatial domain, and the weak statement in matrix notation is rewritten as

$$\mathbf{F}_\beta = \int_\Omega c_\beta \epsilon_\beta \mathbf{N}^{\mathrm{T}} \mathbf{N} \frac{\Delta \mathbf{U}_\beta}{\Delta t} \, dV - \int_\Omega \mathbf{B}^{\mathrm{T}} \mathbf{H}_\beta \, dV - \int_\Omega \left(Q_\beta + R_\beta\right) \mathbf{N}^{\mathrm{T}} \, dV$$
$$+ \int_{\partial\Omega} \overline{H}_\beta \mathbf{N}^{\mathrm{T}} \, d\Gamma = \mathbf{0}, \tag{41a}$$

$$\mathbf{F}_\sigma = \int_\Omega c_\sigma \epsilon_\sigma \mathbf{N}^{\mathrm{T}} \mathbf{N} \frac{\Delta \mathbf{U}_\sigma}{\Delta t} \, dV - \int_\Omega \mathbf{B}^{\mathrm{T}} \mathbf{H}_\sigma \, dV - \int_\Omega (Q_\sigma + R_\sigma) \mathbf{N}^{\mathrm{T}} \, dV$$
$$+ \int_{\partial\Omega} \overline{H}_\sigma \mathbf{N}^{\mathrm{T}} \, d\Gamma = \mathbf{0}, \tag{41b}$$

where $\mathbf{N}$ collects the shape functions associated with all the nodes of the discretized macroscale domain and matrix $\mathbf{B}$ contains derivatives of the shape functions.

The backward Euler method is used for the discretization of the time derivative terms in Eq. (40) (see more details in references [31,35]). In Eq. (41), the temperature increments $\Delta \mathbf{U}_\beta$ and $\Delta \mathbf{U}_\sigma$ are evaluated between the current time step and the last converged time step, and Δt denotes the time step size; the macroscale fluxes $\mathbf{H}_\beta$ and $\mathbf{H}_\sigma$ and the heat sources Q_β and Q_σ are approximated by the values of the current time step.

We now collect the two sets of discrete equations in Eq. (41) and the two field variables in the format of $\mathbf{F} = [\mathbf{F}_\beta \ \mathbf{F}_\sigma]^{\mathrm{T}}$, $\mathbf{U} = [\mathbf{U}_\beta \ \mathbf{U}_\sigma]^{\mathrm{T}}$, respectively. The Newton-Raphson iteration procedure is then employed to solve the system of discrete equations

$$\mathbf{F}(\mathbf{U}_n) = \mathbf{0} \tag{42}$$

at the current time step n ($t = t_n$). The system of linearized equations at iteration step k is expressed as

$$\mathbf{K}(\mathbf{U}_n^{k+1} - \mathbf{U}_n^k) + \mathbf{F}(\mathbf{U}_n^k) = \mathbf{0}, \tag{43}$$

where the global tangent matrix $\mathbf{K}$ is evaluated at iteration step k as

$$\mathbf{K} = \left[\frac{\partial \mathbf{F}}{\partial \mathbf{U}_n}\right]_k = \begin{bmatrix} \mathbf{K}_{\beta\beta} & \mathbf{K}_{\beta\sigma} \\ \mathbf{K}_{\sigma\beta} & \mathbf{K}_{\sigma\sigma} \end{bmatrix}_k. \tag{44}$$

To compute the residual vector $\mathbf{F}$ in Eq. (41), the macroscale fluxes $\mathbf{H}_\beta$ and $\mathbf{H}_\sigma$ at each integration point are directly upscaled from the microscale problem solution and their formulations are presented in Section 4.3 via Eq. (52); likewise, the macroscale heat sources Q_β and Q_σ are obtained through Eq. (53). The tangent matrix $\mathbf{K}$ is calculated from the upscaled tangent matrices $\mathbf{S}_\beta$, $\mathbf{S}_\sigma$, $\mathbf{T}_\beta$, and $\mathbf{T}_\sigma$, and its four components is expressed as

$$\mathbf{K}_{\beta\beta} = \frac{\partial \mathbf{F}_\beta}{\partial \mathbf{U}_\beta} = \int_\Omega \frac{c_\beta \epsilon_\beta}{\Delta t} \mathbf{N}^{\mathrm{T}} \mathbf{N} \, dV - \int_\Omega \mathbf{B}^{\mathrm{T}} \frac{\partial \mathbf{H}_\beta}{\partial \mathbf{U}_\beta} \, dV - \int_\Omega \mathbf{N}^{\mathrm{T}} \frac{\partial Q_\beta}{\partial \mathbf{U}_\beta} \, dV, \tag{45a}$$

$$\mathbf{K}_{\beta\sigma} = \frac{\partial \mathbf{F}_\beta}{\partial \mathbf{U}_\sigma} = -\int_\Omega \mathbf{B}^{\mathrm{T}} \frac{\partial \mathbf{H}_\beta}{\partial \mathbf{U}_\sigma} \, dV - \int_\Omega \mathbf{N}^{\mathrm{T}} \frac{\partial Q_\beta}{\partial \mathbf{U}_\sigma} \, dV, \tag{45b}$$

$$\mathbf{K}_{\sigma\beta} = \frac{\partial \mathbf{F}_\sigma}{\partial \mathbf{U}_\beta} = -\int_\Omega \mathbf{B}^{\mathrm{T}} \frac{\partial \mathbf{H}_\sigma}{\partial \mathbf{U}_\beta} \, dV - \int_\Omega \mathbf{N}^{\mathrm{T}} \frac{\partial Q_\sigma}{\partial \mathbf{U}_\beta} \, dV, \tag{45c}$$

$$\mathbf{K}_{\sigma\sigma} = \frac{\partial \mathbf{F}_\sigma}{\partial \mathbf{U}_\sigma} = \int_\Omega \frac{c_\sigma \epsilon_\sigma}{\Delta t} \mathbf{N}^{\mathrm{T}} \mathbf{N} \, dV - \int_\Omega \mathbf{B}^{\mathrm{T}} \frac{\partial \mathbf{H}_\sigma}{\partial \mathbf{U}_\sigma} \, dV - \int_\Omega \mathbf{N}^{\mathrm{T}} \frac{\partial Q_\sigma}{\partial \mathbf{U}_\sigma} \, dV, \tag{45d}$$

where all the stiffness matrices for the macroscale fluxes ($\mathbf{H}_\beta$ and $\mathbf{H}_\sigma$) and heat sources (Q_β and Q_σ) can be found in Eqs. (B.13) and (B.14).

4.2. Finite element method for microscale problem

The weak form of the microscale governing equation (18) is

$$-\int_{V_\beta} \boldsymbol{\nabla} \delta u_\beta \cdot \left(-k_\beta \boldsymbol{\nabla} u_\beta\right) dV + \int_{\Gamma_{\beta_{ex}} \cup \Gamma_{\beta_\sigma}} \delta u_\beta \mathbf{h}_\beta \cdot \mathbf{n}_\beta \, d\Gamma$$
$$-\int_{V_\beta} \delta u_\beta b_\beta \, dV = 0, \tag{46a}$$

$$-\int_{V_\sigma} \boldsymbol{\nabla}\delta u_\sigma \cdot (-k_\sigma \boldsymbol{\nabla} u_\sigma)\,\mathrm{d}V + \int_{\Gamma_{\sigma ex}\cup\Gamma_{\sigma\beta}} \delta u_\sigma \mathbf{h}_\sigma \cdot \mathbf{n}_\sigma\,\mathrm{d}\Gamma$$

$$-\int_{V_\sigma} \delta u_\sigma b_\sigma\,\mathrm{d}V = 0. \tag{46b}$$

The boundary terms on $\Gamma_{\beta ex}\cup\Gamma_{\beta\sigma}$ and $\Gamma_{\sigma ex}\cup\Gamma_{\sigma\beta}$ do not represent any prescribed Neumann boundary conditions but reflect unknown fluxes caused by the constraints of periodic boundary conditions (24) and temperature continuity condition (25) at the interface. The heat source terms containing b_β and b_σ are also not given but caused by the constraint of consistent temperatures across the macro- and micro-scales (26). All these constraints are enforced through the Lagrange multiplier method, and correspondingly we denote the heat fluxes due to the periodic boundary conditions (24) by $\lambda_{\beta,p}$ and $\lambda_{\sigma,p}$, the heat fluxes due to the temperature continuity condition (25) by $\lambda_{\beta\sigma}$ and $\lambda_{\sigma\beta}$ ($\lambda_{\sigma\beta} = -\lambda_{\beta\sigma}$), and the heat sources due to the consistent temperature constraint (26) by $\lambda_{\beta,b}$ and $\lambda_{\sigma,b}$. The weak form (46) is thus reformulated as

$$\int_{V_\beta} \boldsymbol{\nabla}\delta u_\beta \cdot \left(k_\beta \boldsymbol{\nabla} u_\beta\right)\mathrm{d}V + \int_{\Gamma_{\beta ex}} \delta u_\beta \lambda_{\beta,p}\,d\Gamma + \int_{\Gamma_{\beta\sigma}} \delta u_\beta \lambda_{\beta\sigma}\,d\Gamma$$

$$-\int_{V_\beta} \delta u_\beta \lambda_{\beta,b}\,\mathrm{d}V = 0, \tag{47a}$$

$$\int_{V_\sigma} \boldsymbol{\nabla}\delta u_\sigma \cdot (k_\sigma \boldsymbol{\nabla} u_\sigma)\,\mathrm{d}V + \int_{\Gamma_{\sigma ex}} \delta u_\sigma \lambda_{\sigma,p}\,d\Gamma + \int_{\Gamma_{\sigma\beta}} \delta u_\sigma \lambda_{\sigma\beta}\,d\Gamma$$

$$-\int_{V_\sigma} \delta u_\sigma \lambda_{\sigma,b}\,\mathrm{d}V = 0. \tag{47b}$$

The weak form (47) is further supplemented with the variational forms for the enforcement of the periodic boundary conditions (24) and temperature continuity condition (25):

$$\int_{\Gamma_{\beta ex}\cup\Gamma_{\sigma ex}\cup\Gamma_{\beta\sigma}} \delta\lambda A\,\mathrm{d}\Gamma = 0, \tag{48}$$

where A represents the left-hand formulations of periodic boundary conditions (24) and temperature continuity condition (25).

Inserting the discrete expressions of the field variables and their gradients into the weak form (47) gives the discretized system of governing equations

$$\int_{V_\beta} \mathbf{B}^T k_\beta \mathbf{B}\mathbf{u}_\beta\,\mathrm{d}V + \int_{\Gamma_{\beta ex}} \mathbf{N}^T \lambda_{\beta,p}\,\mathrm{d}\Gamma + \int_{\Gamma_{\beta\sigma}} \mathbf{N}^T \lambda_{\beta\sigma}\,\mathrm{d}\Gamma - \int_{V_\beta} \mathbf{N}^T \lambda_{\beta,b}\,\mathrm{d}V = \mathbf{0}, \tag{49a}$$

$$\int_{V_\sigma} \mathbf{B}^T k_\sigma \mathbf{B}\mathbf{u}_\sigma\,\mathrm{d}V + \int_{\Gamma_{\sigma ex}} \mathbf{N}^T \lambda_{\sigma,p}\,\mathrm{d}\Gamma - \int_{\Gamma_{\sigma\beta}} \mathbf{N}^T \lambda_{\beta\sigma}\,\mathrm{d}\Gamma - \int_{V_\sigma} \mathbf{N}^T \lambda_{\sigma,b}\,\mathrm{d}V = \mathbf{0}. \tag{49b}$$

Conductivities k_β and k_σ are in general temperature dependent, and their derivatives need therefore to be considered in the calculation of the tangent matrices. The equations in Eq. (49) are solved in their own domains where each node has one degree of freedom. The discretization at the interface between the two phases is conforming, but two coinciding nodes, rather than a common node, are assigned with one node for one phase. The temperature continuity and flux continuity constraints are explicitly enforced through Lagrange multipliers between the two coinciding nodes.

The discrete version of the constraints of the periodic boundary conditions (24) and temperature continuity condition (25) is obtained from Eq. (48) by means of the point collocation method [45] and expressed in Eqs. (A.1) to (A.3). The constraint (26) is directly discretized by inserting discrete expressions of the field variables and expressed in Eq. (A.4). These boundary

conditions and constraints, listed in Eqs. (A.1) to (A.4), are expressed in matrix form as

$$\mathbf{A}\mathbf{u} + \mathbf{C}\mathbf{X} = \mathbf{0}, \tag{50}$$

where $\mathbf{u} = [\mathbf{u}_\beta\ \mathbf{u}_\sigma]^T$ collects all the nodal unknowns as concatenation of vectors $\mathbf{u}_\beta$ and $\mathbf{u}_\sigma$, and $\mathbf{A}$ and $\mathbf{C}$ are constant coefficient matrices that can be readily obtained after sorting Eqs. (A.1) to (A.4) consistently with $\mathbf{u}$.

The Lagrange multipliers $\lambda_{\beta,p}$, $\lambda_{\sigma,p}$, and $\lambda_{\beta\sigma}$ representing heat fluxes on the boundaries and interface are discretized in the process of deriving Eqs. (A.1) to (A.3) and stacked together with the two scalar Lagrange multipliers $\lambda_{\beta,b}$ and $\lambda_{\sigma,b}$ in the vector form as $\boldsymbol{\lambda}$. The vector of Lagrange multipliers is then associated with the nodal unknowns $\mathbf{u}$: $\mathbf{w} = [\mathbf{u}\ \boldsymbol{\lambda}]^T$.

The system of nonlinear equations Eq. (49) augmented by Eq. (50) is also solved by the Newton-Raphson iteration scheme as reported in Section 4.1. At iteration step k, the increment of the solution $\Delta\mathbf{w}^{k+1}$ can be computed from

$$\begin{bmatrix} \mathbf{K} & \mathbf{A}^T \\ \mathbf{A} & \mathbf{0} \end{bmatrix}\begin{bmatrix} \Delta\mathbf{u} \\ \Delta\boldsymbol{\lambda} \end{bmatrix} + \begin{bmatrix} \mathbf{f} + \mathbf{A}^T\boldsymbol{\lambda} \\ \mathbf{A}\mathbf{u} + \mathbf{C}\mathbf{X} \end{bmatrix} = \mathbf{0}, \tag{51}$$

where $\mathbf{f}$ represents the vertical stack of the first term of Eq. (49a) and first term of Eq. (49b).

4.3. Upscaling of macroscale quantities

This section details the calculation of the homogenized fluxes ($\mathbf{H}_\beta$ and $\mathbf{H}_\sigma$), the macroscale heat sources (Q_β and Q_σ), and the tangent matrices ($\mathbf{S}_\beta$, $\mathbf{S}_\sigma$, $\mathbf{T}_\beta$, and $\mathbf{T}_\sigma$) based on the microscale finite element solution. By comparison of Eqs. (49) and (51), the Lagrange multipliers $\boldsymbol{\lambda}$ that pertain to the periodic boundary conditions and temperature continuity condition represent the integrals of heat fluxes over the area of influence of each node at the boundary/interface. According to Eq. (33), the macroscale fluxes can be calculated through Lagrange multipliers as:

$$\mathbf{H}_\beta = \frac{1}{V}\int_{\Gamma_{\beta ex}} \left(\mathbf{x}_m \mathbf{N}^T\right)\lambda_{\beta,p}\,\mathrm{d}\Gamma = \frac{1}{V}\mathbf{x}_m \int_{\Gamma_{\beta ex}} \mathbf{N}^T\lambda_{\beta,p}\,\mathrm{d}\Gamma = \frac{1}{V}\mathbf{x}_m \mathbf{A}^T\lambda_{\beta,p}, \tag{52a}$$

$$\mathbf{H}_\sigma = \frac{1}{V}\int_{\Gamma_{\sigma ex}} \left(\mathbf{x}_m \mathbf{N}^T\right)\lambda_{\sigma,p}\,\mathrm{d}\Gamma = \frac{1}{V}\mathbf{x}_m \int_{\Gamma_{\sigma ex}} \mathbf{N}^T\lambda_{\sigma,p}\,\mathrm{d}\Gamma = \frac{1}{V}\mathbf{x}_m \mathbf{A}^T\lambda_{\sigma,p}, \tag{52b}$$

where matrix $\mathbf{x}_m$ is a 2-by-n_m array listing the coordinates of all the n_m nodes of the microscale mesh, $\lambda_{\beta,p}$ and $\lambda_{\sigma,p}$ refer to the components of $\boldsymbol{\lambda}$ that are associated with the periodic boundary conditions (Eqs. (A.1) and (A.2)) imposed on $\Gamma_{\beta ex}$ and on $\Gamma_{\sigma ex}$, respectively. With an abuse of notation, the coefficient matrix $\mathbf{A}^T$ in Eq. (50) needs to be recast here to accommodate $\lambda_{\beta,p}$ and $\lambda_{\sigma,p}$.

The macroscale heat sources due to interfacial heat transfer are computed according to Eqs. (12) and (16) as

$$Q_\beta = -\frac{1}{V}\int_{\Gamma_{\beta\sigma}} \lambda_{\beta\sigma}\,\mathrm{d}\Gamma = -\frac{1}{V}\sum^{\Gamma_{\beta\sigma}} \mathbf{A}^T\lambda_{\beta\sigma}, \tag{53a}$$

$$Q_\sigma = -\frac{1}{V}\int_{\Gamma_{\sigma\beta}} \lambda_{\sigma\beta}\,\mathrm{d}\Gamma = -\frac{1}{V}\sum^{\Gamma_{\sigma\beta}} \mathbf{A}^T\lambda_{\beta\sigma}, \tag{53b}$$

where $\lambda_{\beta\sigma}$ denotes components of $\boldsymbol{\lambda}$ related to the temperature continuity condition (A.3) imposed on nodes on $\Gamma_{\beta\sigma}$ and $\Gamma_{\sigma\beta}$ ($\lambda_{\sigma\beta}$ not discretized). Also, the coefficient matrix $\mathbf{A}^T$ in Eq. 50 is shrunk to accommodate $\lambda_{\beta\sigma}$ but is different in Eqs. (53a) and (53b) because of different nodes on $\Gamma_{\beta\sigma}$ and $\Gamma_{\sigma\beta}$. The coefficient matrices in Eqs. (53a) and (53b) however ensures that $Q_\beta + Q_\sigma = 0$. In

Table 1
Nested two-scale solution procedures of the FE² method.

Macroscale	Microscale
1. Discretize the macroscale domain and Assign an RVE to each integration point	1. Discretize the microscale domain
2. Apply initial conditions to obtain solution U_0 of field variables at $t = t_0$	
3. Use Newton-Raphson iteration to solve Eq. (42) for solution U_n at $t = t_n$	2. Set periodic boundary conditions Eqs. (A1–A5)
(1) Initial guess $U_n^0 = U_{n-1}$	3. Solve microscale problem by Newton-Raphson iteration
(2) Loop over each element and integration point $\xrightarrow{\nabla U_\beta,\ U_\beta,\ \nabla U_\sigma,\ U_\sigma}$	(1) Initial guess: uniform fields ← Eq. (19)
• Assemble residual vector ← homogenized fluxes and heat sources	(2) Assemble stiffness matrix and residual vector
• Assemble stiffness matrix ← tangent matrices $\xleftarrow{\substack{\mathbf{H}_\beta,\ \mathbf{H}_\sigma,\ Q_\beta,\ Q_\sigma \\ \mathbf{S}_\beta,\ \mathbf{S}_\sigma,\ \mathbf{T}_\beta,\ \mathbf{T}_\sigma}}$	(3) Solve Eq. (51) for the increment
(3) Solve the system of equations (43) to calculate the correction and get updated solution U_n^1	(4) Repeat (2)–(3) until convergence achieved
(4) Repeat (2)–(3) until convergence achieved	4. Calculate homogenized fluxes and heat sources, and tangent matrices by Eqs. (52-54)
4. Repeat step 3 for all the time steps $n = 1, 2, 3, …, N$	

Eqs. (52) and (53), all the Lagrange multipliers take the values at the converged state of the microscale iteration.

The tangent matrices of the homogenized fluxes ($\mathbf{H}_\beta$ and $\mathbf{H}_\sigma$) and heat sources (Q_β and Q_σ) with respect to the downscaled quantities $\mathbf{X}$ are derived by applying a small variation to $\mathbf{X}$ and compute the according changes in the flux and source terms. The detailed derivation can be found in Appendix B and the expressions of the tangent matrices are

$$\mathbf{S}_\beta = \frac{\delta \mathbf{H}_\beta}{\delta \mathbf{X}} = \frac{1}{V} \mathbf{x}_m \mathbf{A}^\mathrm{T} \delta_{\beta,\mathrm{p}} \hat{\mathbf{K}}^{-1} \hat{\mathbf{C}}, \quad \mathbf{S}_\sigma = \frac{\delta \mathbf{H}_\sigma}{\delta \mathbf{X}} = \frac{1}{V} \mathbf{x}_m \mathbf{A}^\mathrm{T} \delta_{\sigma,\mathrm{p}} \hat{\mathbf{K}}^{-1} \hat{\mathbf{C}},$$

(54a)

$$\mathbf{T}_\beta = \frac{\delta Q_\beta}{\delta \mathbf{X}} = -\frac{1}{V} \overset{\Gamma_{\beta\sigma}}{\sum} \mathbf{A}^\mathrm{T} \delta_{\beta\sigma} \hat{\mathbf{K}}^{-1} \hat{\mathbf{C}}, \quad \mathbf{T}_\sigma = \frac{\delta Q_\sigma}{\delta \mathbf{X}} = -\frac{1}{V} \overset{\Gamma_{\sigma\beta}}{\sum} \mathbf{A}^\mathrm{T} \delta_{\beta\sigma} \hat{\mathbf{K}}^{-1} \hat{\mathbf{C}}.$$

(54b)

Finally, we summarize the nested two-scale solution procedure in Table 1 for better understanding of the information flow loop between the macro- and micro-scales. Note that the downscaling-upscaling procedure occurs at each iteration step for the solution at any time step, numerically serving the constitutive relation at the macroscale.

5. Results and discussion

We first present some numerical examples for the purpose of validation in Section 5.1 where the FE² simulation results are compared with the results of the single-scale direct numerical simulation (reference solutions). The numerical examples are tailored to show noticeable temperature difference between the two phases and thus to demonstrate the capability of the FE² framework in solving the two-equation model. The first example (Section 5.1.1) focuses on the interfacial heat transfer between the two phases,

which cannot be captured by the one-equation model [27,31], and ignores the spatial diffusion at the macroscale by having a uniform macroscale temperature field. The macroscale spatial heat fluxes are then considered in the second example (Section 5.1.2) that considers both the linear and nonlinear conduction and in the third example (Section 5.1.3) that features a significant conductivity difference. Finally, the microscale RVE simulation results are discussed in Section 5.2 to offer some insights into the interfacial heat transfer coefficient and the microscopic length scale effects.

5.1. Comparison with single-scale simulations

5.1.1. Interfacial heat transfer

Consider the insulated two-phase slab problem studied by Ramos et al. [31] using a one-equation model. As shown in Fig. 3, the two-phase slab consists of a regular array of 140×70 unit cells, with each unit cell consisting of an inclusion (σ phase) embedded in a matrix (β phase). Both phases are isotropic and have constant but different conductivities whose values are listed in Table 2 together with other simulation parameters. The insulated boundary condition $\mathbf{h} = \mathbf{0}$ for $t \in (0, t_{\mathrm{end}}]$ is imposed at the boundary, and the initial condition $u_0 = 0°\mathrm{C}$ is enforced in the whole domain. The simulation time is $t_{\mathrm{end}} = 30\,\mathrm{s}$.

The insulated boundary condition generates a homogeneous temperature field at the macroscale. We can therefore safely use a single square bilinear quadrilateral element with edge length of 0.1m as the macroscale mesh (Fig. 3c). At each integration point of the macroscale element, we take one unit cell as the corresponding RVE. For the single-scale simulation we employ a single unit cell due to the expected homogeneity of the solution fields. From the single-scale simulation, the intrinsic average of the temperatures of the β and σ phases over the unit cell are defined as $\bar{u}_\beta$ and $\bar{u}_\sigma$, according to Eq. (2), and serve as references for the two macroscale solutions U_β and U_σ, respectively. Moreover, the aver-
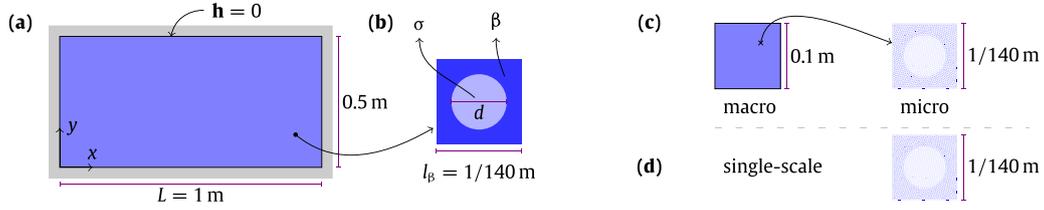
Fig. 3. An insulated two-phase slab (a) with width 1m and height 0.5m. The slab consists of a regular arrangement of unit cells (140×70); each unit cell (b) with edge length $l_\beta = 1/140$ m consists of two phases (β and σ). The diameter of the inclusion (σ phase) is $d = 0.65\, l_\beta$. The initial temperature is 0°C everywhere and heat is generated in the σ phase; all the parameters are listed in Table 2. Panel (c) shows the computational mesh for the FE^2 method: a square bilinear quadrilateral element is used for the macroscale mesh and 2436 linear triangular elements for the RVE mesh. The single-scale discretization of a unit cell in panel (d) is the same as that of the RVE.
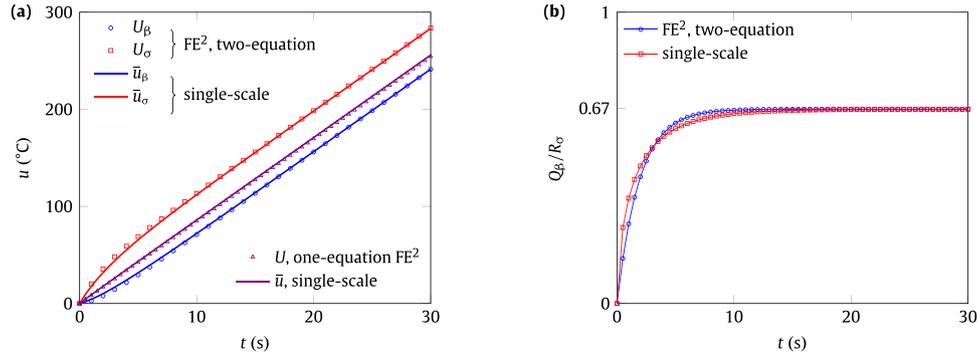
Fig. 4. Comparison between the FE^2 simulation results and the results of the single-scale simulations. (a) Temperature increases with time due to the heat generation in the inclusion. The macroscale temperatures U_β and U_σ are obtained from the two-equation model with the FE^2 framework, while U is from the one-equation model. The average temperatures $\bar{u}_\beta$ and $\bar{u}_\sigma$ are intrinsic averages over the β and σ phases of the unit cell, respectively, and $\bar{u}$ refers to the average over the whole unit cell as defined in Eq. (55). (b) Volumetric interfacial heat transfer Q_β normalized by the given volume-averaged heat source R_σ (Table 2).

age temperature $\bar{u}$ of the whole unit cell, defined as

$$\bar{u} = \epsilon_\beta \bar{u}_\beta + \epsilon_\sigma \bar{u}_\sigma, \tag{55}$$

is compared to the solution of the one-equation model in Eq. (35), which is independently obtained from the FE^2 method and not calculated as the weighted average of U_β and U_σ by Eq. (39).

The FE^2 simulation results are compared with results from the single-scale simulation in Fig. 4. The macroscale temperature fields U_β and U_σ, defined in Eqs. (7) and (14), agree with the average temperatures $\bar{u}_\beta$ and $\bar{u}_\sigma$ predicted by the single-scale simulation (Fig. 4a), respectively. The macroscale temperature U obtained with the one-equation model agrees with the average temperature $\bar{u}$ of the whole unit cell obtained with the single-scale simulation. As $\bar{u}$ is the weighted average of $\bar{u}_\beta$ and $\bar{u}_\sigma$ (Eq. (55)), it is inferred that U matches with the weighted average of U_β and U_σ: Eq. (39) holds. This agreement numerically validates the relation between the two models: the one-equation model is a special case of the two-equation model, as shown in Section 3.5.

Fig. 4 b shows the temporal evolution of the interfacial heat transfer Q_β (Eq. (12)) normalized by the given heat source R_σ (Eq. (15)): it increases sharply in the beginning and then quickly stabilizes. In this example, the heat is generated in the σ phase and partially flows into the β phase, increasing the temperatures of both phases simultaneously. The normalized interfacial heat transfer measures the fraction of the heat generation R_σ that goes to the matrix (the β phase). In the plateau stage, the normalized heat transfer converges to the volume fraction of the β phase, suggesting that the distribution of the heat generation between the two phases reaches an equilibrium and is determined by the volume fraction. Again, the agreement between the FE^2 simulation results and results of the single-scale simulation validates the computational framework for the two-equation model.

Actually, the temperature difference between the two phases, as shown above, is also of interest to Ramos et al. [31] and shown in Fig. 12 of their paper. However, since they used the one-equation
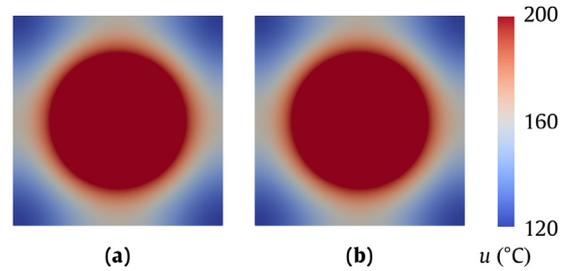
Fig. 5. Temperature profile at $t = 20$ s in (a) an RVE from the microscale FE simulation and (b) in the unit cell from the single-scale simulation.

model, the temperature difference at the macroscale was not presented; instead, they reported the temperatures of a "hot" point in the σ phase and a "cold" point in the β phase of an RVE.

The temperature profile in an RVE (Fig. 5a) by our FE^2 simulation also resembles the temperature profile in the unit cell (Fig. 5b) obtained with the single-scale simulation. The temperature variation in each phase can be reproduced in our two-equation model thanks to the transfer of the two macroscale temperatures to the microscale RVE (Eq. (26)) and the microscale boundary conditions. The one-equation model will however yield a uniform RVE temperature field as shown in Fig. 13a of Ramos et al. [31] unless the microscale transient effect is taken into account (Fig. 13b of Ramos et al. [31]).

5.1.2. Nonlinear heat conduction

This example considers the same two-phase medium as in Fig. 3a and b but with different boundary conditions in order to allow for heat conduction at the macroscale, as shown in Fig. 6a. Neumann boundary conditions are enforced at the horizontal edges, while Dirichlet boundary conditions are imposed at
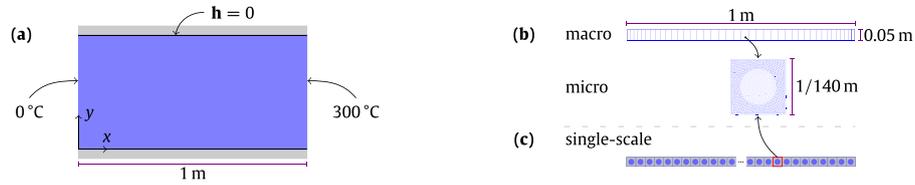
Fig. 6. (a) The same two-phase slab as in Fig. 3, but with different boundary conditions. In this case the slab is insulated at the upper and lower edges and constant temperatures are applied at the left- and right-hand edges. The initial temperature is 0°C everywhere. (b) For the FE^2 simulation, the macroscale mesh consists of 40 bilinear quadrilateral elements and the mesh is denser at the two sides; the microscale RVE mesh is the same as the RVE mesh in Fig. 3. (c) The single-scale simulation is performed on a mesh consisting of a layer of 140 side-by-side unit cells, each discretized as the RVE.
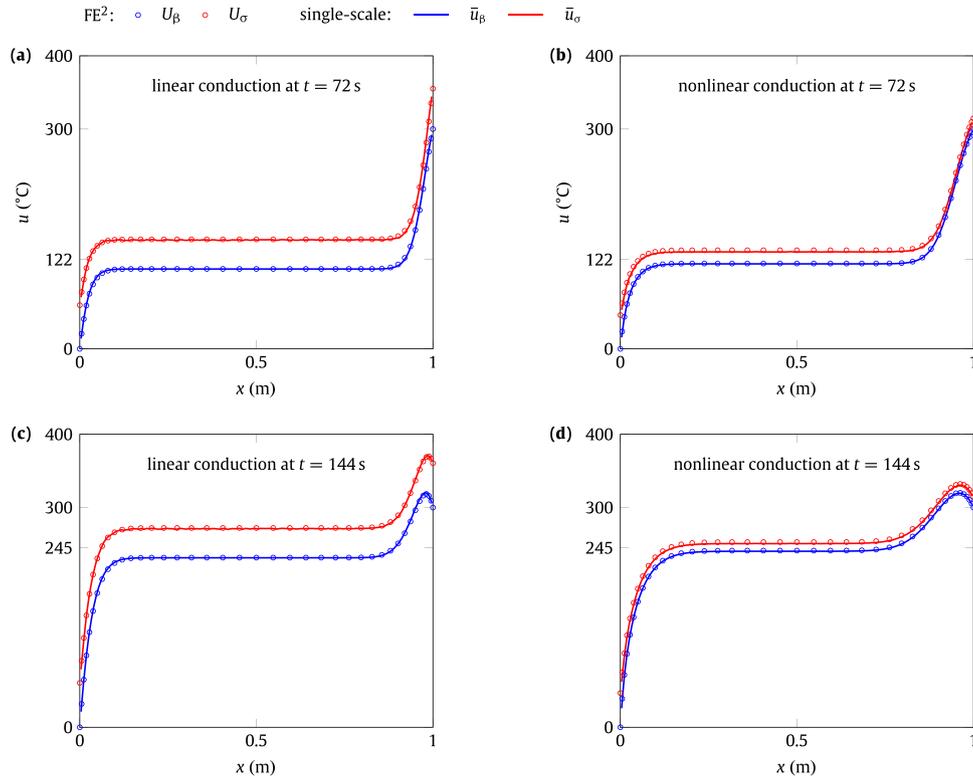
Fig. 7. Comparison between the FE^2 and single-scale simulation results. Panels (a) and (c) show the results for the linear conduction case and panels (c) and (d) for the nonlinear conduction case. Quantities U_β and U_σ refer to the macroscale solutions (FE^2 method), while $\bar{u}_\beta$ and $\bar{u}_\sigma$ indicate the intrinsic averages of the temperature in each phase (single-scale approach).
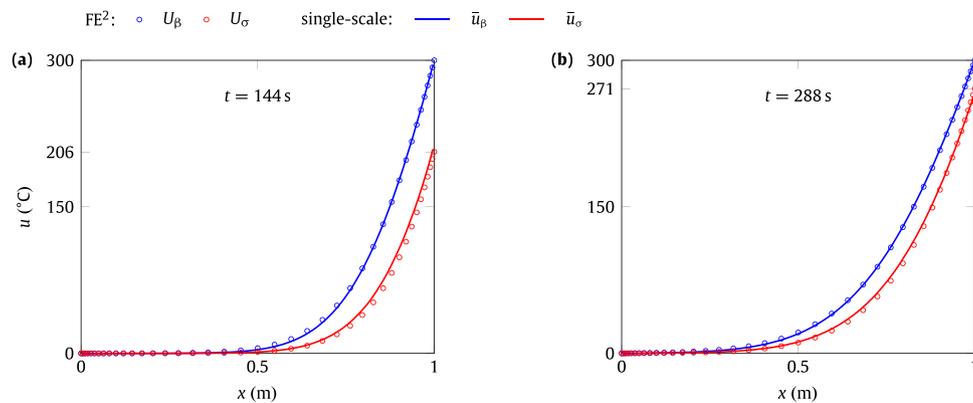
Fig. 8. Comparison between the FE^2 and single-scale simulation results for the conduction problem characterized by a significant conductivity difference in the two phases. Quantities U_β and U_σ refer to the macroscale solutions (FE^2 method), while $\bar{u}_\beta$ and $\bar{u}_\sigma$ indicate the intrinsic averages of the temperature in each phase (single-scale approach).

Table 2
Parameters of the FE^2 multi-scale and single-scale simulations for Fig. 4.

		quantity	symbol	unit	phase β	phase σ
Multi-scale	macro	volume fraction	ϵ	-	0.67	0.33
		volumetric heat capacity	c	J/(m^{3}K)	3.51×10^6	3.51×10^6
		volume-averaged heat source[a]	R	W/m^3	0.0	2.99×10^7
	micro	conductivity	k	W/(mK)	1.0	4.0×10^2
Single-scale		volumetric heat capacity	c	J/(m^{3}K)	3.51×10^6	3.51×10^6
		volumetric heat source	r	W/m^3	0.0	9.0×10^7
		conductivity	k	W/(mK)	1.0	4.0×10^2

[a] This quantity is calculated according to Eq. (9) or (15).

Table 3
Parameters of the FE^2 multi-scale and single-scale simulations for Fig. 7.

		quantity	symbol	unit	phase β	phase σ
multi-scale	macro	volume fraction	ϵ	-	0.67	0.33
		volumetric heat capacity	c	J/(m^{3}K)	1.76×10^7	1.76×10^7
		volume-averaged heat source	R	W/m^3	0.0	2.99×10^7
	micro	conductivity[a]	k	W/(mK)	$400 + k_0 T$	$1 + k_1 T$
single-scale		volumetric heat capacity	c	J/(m^{3}K)	1.76×10^7	1.76×10^7
		volumetric heat source	r	W/m^3	0.0	9.0×10^7
		conductivity[a]	k	W/(mK)	$400 + k_0 T$	$1 + k_1 T$

[a] Coefficients $k_0 = k_1 = 0$ for the linear conduction case while $k_0 = 4$ and $k_1 = 0.01$ for the nonlinear conduction case; T is the value of temperature measured in degrees Celsius and ranges from 0 to 400.

the vertical edges:

$$\mathbf{h}|_{y=0} = \mathbf{0}, \qquad \mathbf{h}|_{y=0.5\,\mathrm{m}} = \mathbf{0} \qquad \text{and}$$
$$u|_{x=0} = 0°\mathrm{C}, \qquad u|_{x=1\,\mathrm{m}} = 300°\mathrm{C} \qquad \text{for } t \in (0, t_{\mathrm{end}}],$$

where $t_{\mathrm{end}} = 288\,$s. The initial condition $u_0 = 0°\,$C is enforced in the whole domain. As these boundary conditions ensure a uniform macroscale temperature field along the y direction, we only consider one row of 40 bilinear quadrilateral elements for the macroscale mesh (Fig. 6b). For the RVE we use one unit cell, the same as in Fig. 3c. Considering the insulated top and bottom boundaries, we also simulate one layer of unit cells for the single-scale simulation (i.e., 140 side-by-side unit cells as shown in Fig. 6c). Each unit cell has the same mesh as the RVE.

To have distinct temperature difference between the two phases, a heat source in the σ phase is also contained to maintain the local thermal non-equilibrium condition [3,12]. This scenario is analogous to the real transport problem with reaction sources in the biofilm phase in chemical engineering applications [5,6] where a local mass non-equilibrium condition arises. As the FE^2 method is advantageous in addressing general constitutive relations, here we not only simulate the linear conduction problem with constant conductivities but also a nonlinear conduction problem with temperature-dependent conductivities. The corresponding parameters are listed in Table 3.

As shown in Fig. 7, the FE^2 simulation results can capture the temperature distribution and evolution in the two phases and agree well with the results of the single-scale simulation for both the linear and nonlinear conduction cases. In Fig. 7a and c for the linear conduction case, the temperature of the slab continuously increases because of the heat generated in the σ phase but remains constant at the left- and right-hand boundaries as specified. Two typical time instants are selected to show the evolution of the temperature profile. At 72s, the temperature increase due to the heat generation is uniform in the middle (from 0.1 to 0.9m) of the slab; close to the two vertical edges of the slab, high temperature gradients develop due to the boundary condition of fixed temperatures. At 144s, a temperature peak is observed near the right-hand vertical edge because the heat accumulated from the heat source cannot be fluxed out timely. In the FE^2 simulation, the boundary conditions of fixed temperatures at the two vertical edges (Fig. 6a) are only applied to the β phase at the macroscale; for the σ phase,

the leftmost and rightmost boundaries are also insulated and its temperature U_σ is determined by the interaction with the β phase as well as the internal heat generation. This setting enables the FE^2 method to capture the phenomenon that the temperatures of the σ phase at the two vertical edges are higher than those of the β phase.

The arguments exposed above also apply to the case of nonlinear conduction as shown in Fig. 7b and d, with minor differences. According to Table 3, the conductivities in the nonlinear case are always higher than those in the linear case, and thus the temperature differences between the two phases are smaller and the temperature gradients near the two vertical edges are lower (Fig. 7a vs b and Fig. 7c vs d). At each time instant, the weighted averages of U_β and U_σ according to Eq. (39) in the middle of the slab however remain unchanged for the linear and nonlinear cases because they are determined by the heat generation and can be manually calculated and checked.

It is remarked that, for nonlinear conduction problems, the principle of scale separation needs to be checked more carefully. According to Quintard et al. [46] and Hager and Whitaker [47], the length scale of the variation of macroscale field variables has to be much larger than the characteristic length scale of the RVE for proper evaluation of the nonlinear constitutive relation at the macroscale. Similarly, Geers et al. [37] emphasized that "large spatial gradients at the macro-scale cannot be resolved" by the first-order homogenization due to the restriction of the scale separation principle.

5.1.3. Significant conductivity difference

We further consider another scenario that does not include a heat source but features a significant difference in the conductivity between the two phases, also resulting in a temperature difference. The same problem setting as in Fig. 6 is used here but a different set of parameters is taken and listed in Table 4. This situation is representative of the heat transfer into a composite material composed of a highly conductive matrix but poorly conductive inclusions. A certain amount of time is necessary before both phases attain the same temperature [15].

Fig. 8 shows the simulation results of the FE^2 method and the single-scale approach. The fixed temperature at the right-hand side is higher than the initial null temperature of the whole slab, lead-

Table 4
Parameters of the FE^2 multi-scale and single-scale simulations for Fig. 8.

		quantity	symbol	unit	phase β	phase σ
multi-scale	macro	volume fraction	ϵ	-	0.67	0.33
		volumetric heat capacity	c	J/(m^{3}K)	1.76×10^7	1.76×10^7
		volume-averaged heat source	R	W/m^3	0.0	0.0
	micro	conductivity	k	W/(mK)	4.0×10^3	1.0×10^{-1}
single-scale		volumetric heat capacity	c	J/(m^{3}K)	1.76×10^7	1.76×10^7
		volumetric heat source	r	W/m^3	0.0	0.0
		conductivity	k	W/(mK)	4.0×10^3	1.0×10^{-1}
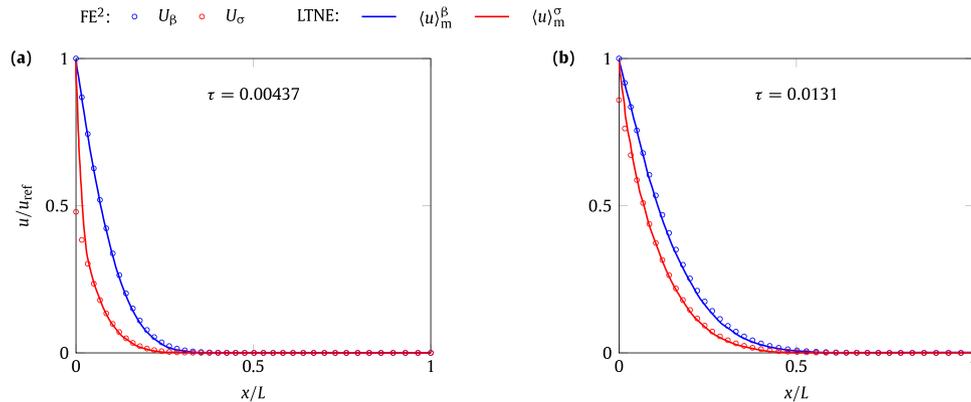
Fig. 9. Comparison between the FE^2 method and local thermal non-equilibrium model (LTNM) at two dimensionless time instants τ. Quantities U_β and U_σ refer to the macroscale solutions (FE^2 method), while $\langle u \rangle_m^\beta$ and $\langle u \rangle_m^\sigma$ are the intrinsic averages of the temperature of the two phases obtained from the LTNM as reported in Fig. 24 of Quintard and Whitaker [1].

ing to heat influx at the right-hand side as time passes. Since the matrix (β phase) is much more conductive than the inclusion (σ phase), the matrix's temperature is always higher than the temperature of the inclusion, to the extent that an evident temperature difference is observed. At two time instants, the FE^2 simulation results agree with those by the single-scale simulation, validating the FE^2 multi-scale framework for the two-equation model.

All the previous comparisons are against the single-scale direct numerical simulations, and next we present the comparison between the FE^2 results and the predictions by a two-phase local thermal non-equilibrium model (LTNM). In particular, we consider the example shown in Fig. 24 of Quintard and Whitaker [1]. The key parameters are adapted and reported below (readers are referred to Table II of the reference for further details): the macroscale length is $L = 10$ m while the RVE edge length is $l_\beta = 1$ m; the volume fraction of the matrix phase β is 0.62; the conductivity ratio of the two phases is $k_\beta/k_\sigma = 100$ where $k_\beta = 1$ W/(mK). The temperature U_β is specified to be T_{ref} at the left-hand boundary and null at the right-hand boundary. The difference from the LTNM lies in the boundary condition for the temperature U_σ at the left- and right-hand boundaries: the FE^2 method does not fix U_σ at the boundaries as the LTNM did; instead, it uses insulated boundaries. This choice is consistent with the actual geometry that the inclusions (σ phase) only have interfacial boundaries with the matrix (β phase) and the temperature U_σ is driven by the interaction with the matrix (see Section 5.1.2 and Fig. 7).

The comparison is shown in Fig. 9 at two scaled time instants. The results from these two approaches are quite close, except for the data point denoting temperature U_σ at the leftmost boundary because of the different boundary settings. The agreement can be explained by the same heat transfer coefficient value (0.25) extracted from the tangent matrices for interfacial heat transfer by the FE^2 method as the one reported in Quintard and Whitaker [1] (see Eq. (56) and the following section 5.2 for more discussions). This comparison further validates the FE^2 method in

terms of the microscale problem simulation and calculation of the homogenized quantities and their tangent matrices.

In spite of the good agreement with the LTNM, the scale difference ($l_\beta/L = 0.1$) in this example is too small to be suitable for the FE^2 method: the RVE size and the macroscale element size are almost in the same magnitude, which basically does not satisfy the principle of scale separation. The single-scale direct numerical simulation is pragmatically more appropriate in such case. The small scale difference (or relatively too large RVE) may also explain the discrepancy between the single-scale simulation results of the σ phase and predictions by the multi-scale approaches [1], which is not shown here as the comparison is not well justified.

5.2. Insights from microscale RVE simulations

In the previous simulations of linear conduction problems, we observe that in the tangent vector $\mathbf{T}_\beta$ (Eq. (54b)), the third component that shows dependence of the interfacial heat flow on U_β is always the additive inverse of the sixth component that shows dependence on U_σ: $\mathbf{T}_\beta^{(3)} + \mathbf{T}_\beta^{(6)} = 0$. This relation is also observed, as expected, in $\mathbf{T}_\sigma$. The other components are relatively negligible, implying almost no temperature gradient dependence of the interfacial heat flow. Moreover, the components of $\mathbf{T}_\beta$ themselves are independent of the macroscale temperatures U_β and U_σ. These observations suggest that the volumetric interfacial heat flow Q_β as defined in Eq. (12) linearly depends on the temperature difference between the two phases according to the relationship

$$Q_\beta = T_h \left(U_\sigma - U_\beta \right), \tag{56}$$

where T_h is usually referred to as the interfacial heat transfer coefficient [1,3,4]. The linear dependence in Eq. (56) can also be deduced from the results reported in Fig. 4: the ratio between Q_β and $U_\beta - U_\sigma$ yields, at each time step, the same coefficient T_h values. Although the linear relation (56) has been widely used in the homogenized transport equations in the two-equation model [1,4,9],
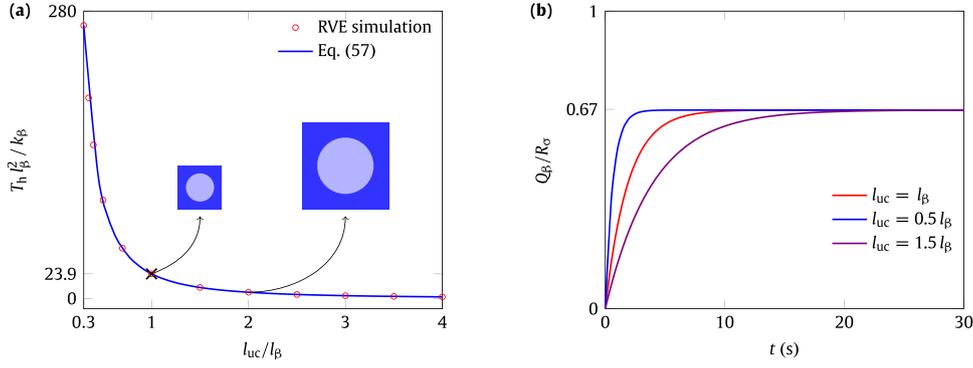
Fig. 10. Effect of unit cell size: (a) interfacial heat transfer coefficient T_h decreases quadratically with the unit cell edge length l_{uc}; (b) increase of the interfacial heat transfer with time at three different unit cell sizes. The values of l_β, k_β, and R_σ can be found in Section 5.1.1.

the estimation of the heat transfer coefficient value is however still challenging [8] either in experimental measurements [4] or by analytical approaches [1]. Our numerical results suggest that the heat transfer coefficient is indeed constant for a linear two-phase system. The microscale RVE simulation thus numerically validates the widely-used linear relation and, more importantly, offers a convenient way to calculate the heat transfer coefficient.

The relation $\mathbf{T}_\beta^{(3)} + \mathbf{T}_\beta^{(6)} = 0$ observed in the linear examples however breaks down in the nonlinear conduction case and the linear relation (56) does not hold. The heat transfer coefficient defined in the linear case actually depends on the specific conductivities of both phases. In nonlinear conduction problems, the temperature dependent conductivity naturally leads to temperature dependent coefficients $\mathbf{T}_\beta^{(3)}$ and $\mathbf{T}_\beta^{(6)}$. Compared to the numerical approach by Quintard and Whitaker [1], the proposed FE^2 framework has the intrinsic advantage of addressing nonlinear conduction problems because the interfacial heat transfer as well as its dependence on macroscale field variables are numerically calculated from the microscale problem, avoiding the postulation of relation (56) and the wide range of values reported for the heat transfer coefficient [8].

In conventional FE^2 frameworks for the one-equation model, the effective conductivity of the whole RVE is generally not affected by the microscopic length scale, given that material properties of each phase are fixed. An analogous situation arises in computational solid mechanics: the homogenized stiffness (deformation gradient dependence of the homogenized stress) does not depend on the unit cell size. This microscopic length scale independence is also true for the tangent matrices ($\mathbf{S}_\beta$ and $\mathbf{S}_\sigma$) characterizing the temperature gradient dependence of the homogenized flux, provided that volume fraction and conductivity of each phase are fixed. However, this conclusion does not apply to the coefficient T_h of the interfacial heat transfer. Figure 10a shows that the coefficient T_h depends on the edge length of the unit cell l_{uc} that characterizes the microscopic length scale. As l_{uc} increases, the coefficient T_h decreases in a non-linear fashion which can be described with good approximation by the quadratic expression

$$\frac{T_h l_\beta^2}{k_\beta} = \frac{a}{\left(l_{uc}/l_\beta\right)^2} \tag{57}$$

between T_h and l_{uc}. The quadratic relation was also reported in Table 1 of Quintard and Whitaker [1]. Our simulation results can be fit by Eq. (57) with the same coefficient ($a = 25.8$) reported by Quintard and Whitaker [1] if the same parameters (volume fraction and conductivity of each phase) are used in our simulations. These results further indicate that our numerical framework can properly account for linear conduction effects in a two-phase medium.
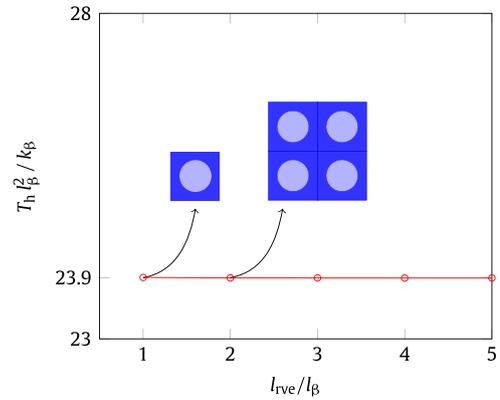
Fig. 11. Effect of RVE size: the interfacial heat transfer coefficient T_h in Eq. (56) remains constant for different RVE sizes l_{rve}.

Fig. 10b shows the effect of the microscopic length scale on the evolution of the interfacial heat transfer in the example of Section 5.1.1. The smaller the unit cell, the faster the interfacial heat transfer increases with time in the transient stage and the earlier it begins to level off. The microscopic length scale however does not affect the magnitude of the normalized interfacial heat transfer in the plateau stage, which is determined by the volume fraction. Since a smaller unit cell corresponds to a greater value of the coefficient T_h (Eq. (57)), the temperature difference will be smaller according to Eq. (56), in view of the same interfacial heat transfer in the plateau stage. Eventually, with increasingly smaller unit cells, the temperature difference will be as small as to the extent that the local equilibrium assumption holds [19]. The microscale FE simulation can thus provide quantitative guidelines for the determination of the microscopic length scale at which the one-equation model can be used with confidence (i.e., by accepting a controllable error) in place of the two-equation model.

The unit cell size is not to be confused with the RVE size. The unit cell size characterizes the microscopic length scale and thus is determined by the material, while the RVE is associated with the FE^2 method and its size is determined so that the RVE is as large as to be representative but also as small as to satisfy the rule of scale separation. The difference between a larger unit cell and a larger RVE can be seen in Figs. 10a and 11. Unlike unit cells, larger RVEs however do not affect the results for the two-phase medium used in this study: as shown in Fig. 11, the interfacial heat transfer coefficient T_h remains unchanged with the RVE size l_{rve}. Our numerical results also indicate that the tangent matrices $\mathbf{S}_\beta$ and $\mathbf{S}_\sigma$ of the homogenized flux (effective conductivities) do not change with

the RVE size. Therefore, a single unit cell can be safely used as the RVE in our studies.

6. Conclusion

For transient heat conduction in a two-phase medium, this study presents an FE^2 two-scale framework that can properly address the local thermal non-equilibrium condition thanks to the use of a two-equation model. The approach has been demonstrated in simple academic problems with the intention of showing its potential in addressing general problems. The FE^2 method does not explicitly require the definition of constitutive relations or the employment of other conditions, such as the interfacial heat transfer condition (56), at the macroscale. The microscale problem enables the use of general constitutive relations (e.g., temperature dependent conductivity) leading to the solution of general nonlinear transport problems. The heat transfer coefficient, expressing the macroscale temperature dependence of the interfacial heat transfer in the linear case, is found to depend on the microscopic length scale, which is a unique and new feature of the proposed FE^2 method.

The simple numerical examples are limited to two-dimensional ordered porous media, and three-dimensional disordered porous microstructures need to be considered for further validation of the FE^2 approach. A two-dimensional setting does not allow both the matrix and inclusion domains to be path-connected in both the x and y directions; with path-connected matrix, the inclusions are often "isolated" from each other. This restriction leads to null effective transport properties of the inclusion phase at the macroscale. A three-dimensional geometry can avoid this constraint and thus is highly anticipated. The present model derivation and finite element procedures are actually general regardless of the problem dimension and RVE geometrical morphology; they are, in principle, readily to be applied to three-dimensional porous microstructures with some modifications of numerical implementation of the periodic boundary conditions in a three-dimensional setting.

This study is also restricted to simple interfacial conditions (temperature and flux continuities), and more general interfacial constraints (e.g., Butler-Volmer relation) between the two phases in terms of field variables and fluxes should be further explored so that the FE^2 approach can be applied to real-life problems such as the species transport in battery electrodes.

Declaration of Competing Interest

The authors declare that they have no known competing financial interests or personal relationships that could have appeared to influence the work reported in this paper.

Acknowlgedgments

Appendix A. Microscale problem boundary conditions

1. Periodic boundary conditions As shown in Fig. 1b, we group the external boundaries into the master boundary $\Gamma_{lb} = \Gamma_l \cup \Gamma_b$ and slave boundary $\Gamma_{rt} = \Gamma_r \cup \Gamma_t$. The enforcement of the periodic boundary conditions requires a one-to-one correspondence between the master and slave boundaries ($\Gamma_l \leftrightarrow \Gamma_r$; $\Gamma_b \leftrightarrow \Gamma_t$) for each phase in terms of mesh nodes. The constraint in Eq. (24) is then applied to each pair of nodes, one node

on the master boundary and the other on the slave boundary, excluding the four corner nodes. The total number of node pairs is denoted by N_{pb}. For each pair of nodes, we assign a Lagrange multiplier λ_l to the constraint between them, with the Lagrange constraint equation expressed as

$$u_\alpha^l\big|_{\Gamma_{lb}} - u_\alpha^l\big|_{\Gamma_{rt}} - \boldsymbol{\nabla} U_\alpha \cdot \left(\mathbf{x}_{\Gamma_{lb}}^l - \mathbf{x}_{\Gamma_{rt}}^l\right) = 0, \tag{A.1}$$

where l ranges from 1 to N_{pb}, and α refers to either β or σ depending on the phase to which the node pair l belongs. For the four corner nodes, the three Lagrange constraint equations are

$$\begin{aligned} u_\alpha^{(2)} - u_\alpha^{(1)} - \boldsymbol{\nabla} U_\alpha \cdot \left(\mathbf{x}^{(2)} - \mathbf{x}^{(1)}\right) &= 0, \\ u_\alpha^{(3)} - u_\alpha^{(1)} - \boldsymbol{\nabla} U_\alpha \cdot \left(\mathbf{x}^{(3)} - \mathbf{x}^{(1)}\right) &= 0, \\ u_\alpha^{(4)} - u_\alpha^{(1)} - \boldsymbol{\nabla} U_\alpha \cdot \left(\mathbf{x}^{(4)} - \mathbf{x}^{(1)}\right) &= 0, \end{aligned} \tag{A.2}$$

where α takes the phase (either β or σ) containing the corner nodes.

2. Interfacial boundary conditions
If there are N_{if} pairs of interface nodes, there exist N_{if} Lagrange constraint equations

$$u_\beta^l - u_\sigma^l = 0, \tag{A.3}$$

where l ranges from 1 to N_{if}, u_β^l denotes the nodal temperature at the interface $\Gamma_{\beta\sigma}$, and u_σ^l is the temperature of the corresponding node on $\Gamma_{\sigma\beta}$.

3. Conservation of the stored heat between the macro- and microscales
This condition is expressed by means of two Lagrange constraint equations from Eq. (26):

$$\int_{V_\beta} \mathbf{N}\,dV\,\mathbf{u}_\beta - V_\beta U_\beta = 0, \; \int_{V_\sigma} \mathbf{N}\,dV\,\mathbf{u}_\sigma - V_\sigma U_\sigma = 0. \tag{A.4}$$

In total, the number of Lagrange multipliers is

$$N_\lambda = N_{pb} + N_{if} + 5, \tag{A.5}$$

i.e., the sum of Lagrange multipliers from Eqs. (A.1) to (A.4).

Appendix B. Calculation of tangent matrices

The tangent matrices of the macroscale fluxes and heat sources with respect to the downscaled macroscale quantities (Section 4.3) are derived as follows. At a converged state, the increment $\Delta \mathbf{w}$ in Eq. (51) is zero, and hence the residual vector

$$\hat{\mathbf{f}} = \begin{bmatrix} \mathbf{f} + \mathbf{A}^T\lambda \\ \mathbf{A}\mathbf{u} + \mathbf{C}\mathbf{X} \end{bmatrix} = \mathbf{0}. \tag{B.1}$$

We then apply a small variation $\delta \mathbf{X}$ to the macroscale quantities $\mathbf{X}$ and compute the corresponding change in the microscale solution. Note that Eq. (B.1) should always hold to get the converged microscale solution. Therefore, we have

$$\delta\hat{\mathbf{f}} = \mathbf{0} = \begin{bmatrix} \mathbf{K} & \mathbf{A}^T \\ \mathbf{A} & \mathbf{0} \end{bmatrix}\begin{bmatrix} \delta\mathbf{u} \\ \delta\lambda \end{bmatrix} + \begin{bmatrix} \mathbf{0} \\ \mathbf{C} \end{bmatrix}\delta\mathbf{X}. \tag{B.2}$$

Rearranging Eq. (B.2), we obtain

$$\begin{bmatrix} \mathbf{K} & \mathbf{A}^T \\ \mathbf{A} & \mathbf{0} \end{bmatrix}\begin{bmatrix} \delta\mathbf{u} \\ \delta\lambda \end{bmatrix} = -\begin{bmatrix} \mathbf{0} \\ \mathbf{C} \end{bmatrix}\delta\mathbf{X}. \tag{B.3}$$

To solve Eq. (B.3), we rewrite it as

$$\hat{\mathbf{K}}\delta\mathbf{w} = \hat{\mathbf{C}}\delta\mathbf{X} \tag{B.4}$$

and thus the variation $\delta\mathbf{w}$ is expressed as

$$\delta\mathbf{w} = \hat{\mathbf{K}}^{-1}\hat{\mathbf{C}}\delta\mathbf{X}, \tag{B.5}$$

where $\hat{\mathbf{K}}^{-1}$ must be evaluated at the converged state of the microscale iteration. The solution $\delta\lambda$ is extracted from $\delta\mathbf{w}$ by means of the gather matrix δ:

$$\delta\lambda = \delta\delta\mathbf{w}. \tag{B.6}$$

According to Eqs. (B.5) and (B.6), the variations of the homogenized fluxes (52) can be formulated as

$$\delta \mathbf{H}_\beta = \frac{1}{V} \mathbf{x}_m \mathbf{A}^T \delta \lambda_{\beta,p} = \frac{1}{V} \mathbf{x}_m \mathbf{A}^T \delta_{\beta,p} \hat{\mathbf{K}}^{-1} \hat{\mathbf{C}} \delta \mathbf{X}, \tag{B.7a}$$

$$\delta \mathbf{H}_\sigma = \frac{1}{V} \mathbf{x}_m \mathbf{A}^T \delta \lambda_{\sigma,p} = \frac{1}{V} \mathbf{x}_m \mathbf{A}^T \delta_{\sigma,p} \hat{\mathbf{K}}^{-1} \hat{\mathbf{C}} \delta \mathbf{X}, \tag{B.7b}$$

where $\delta_{\beta,p}$ and $\delta_{\sigma,p}$ are the gather matrices used to retrieve $\lambda_{\beta,p}$ and $\lambda_{\sigma,p}$, respectively, from λ. The variations of the macroscale heat sources (53) due to interfacial heat transfer are calculated as

$$\delta Q_\beta = -\frac{1}{V} \sum^{\Gamma_{\beta\sigma}} \mathbf{A}^T \delta \lambda_{\beta\sigma} = -\frac{1}{V} \sum^{\Gamma_{\beta\sigma}} \mathbf{A}^T \delta_{\beta\sigma} \hat{\mathbf{K}}^{-1} \hat{\mathbf{C}} \delta \mathbf{X}, \tag{B.8a}$$

$$\delta Q_\sigma = -\frac{1}{V} \sum^{\Gamma_{\sigma\beta}} \mathbf{A}^T \delta \lambda_{\beta\sigma} = -\frac{1}{V} \sum^{\Gamma_{\sigma\beta}} \mathbf{A}^T \delta_{\beta\sigma} \hat{\mathbf{K}}^{-1} \hat{\mathbf{C}} \delta \mathbf{X}, \tag{B.8b}$$

where $\delta_{\beta\sigma}$ is the gather matrix used to retrieve $\lambda_{\beta\sigma}$ from λ. The tangent matrices for the macroscale heat fluxes are calculated as

$$\mathbf{S}_\beta = \frac{\delta \mathbf{H}_\beta}{\delta \mathbf{X}} = \frac{1}{V} \mathbf{x}_m \mathbf{A}^T \delta_{\beta,p} \hat{\mathbf{K}}^{-1} \hat{\mathbf{C}}, \tag{B.9a}$$

$$\mathbf{S}_\sigma = \frac{\delta \mathbf{H}_\sigma}{\delta \mathbf{X}} = \frac{1}{V} \mathbf{x}_m \mathbf{A}^T \delta_{\sigma,p} \hat{\mathbf{K}}^{-1} \hat{\mathbf{C}}, \tag{B.9b}$$

and the tangent matrices for the macroscale heat sources due to interfacial heat transfer are expressed as

$$\mathbf{T}_\beta = \frac{\delta Q_\beta}{\delta \mathbf{X}} = -\frac{1}{V} \sum^{\Gamma_{\beta\sigma}} \mathbf{A}^T \delta_{\beta\sigma} \hat{\mathbf{K}}^{-1} \hat{\mathbf{C}}, \tag{B.10a}$$

$$\mathbf{T}_\sigma = \frac{\delta Q_\sigma}{\delta \mathbf{X}} = -\frac{1}{V} \sum^{\Gamma_{\sigma\beta}} \mathbf{A}^T \delta_{\beta\sigma} \hat{\mathbf{K}}^{-1} \hat{\mathbf{C}}. \tag{B.10b}$$

The above-derived tangent matrices are formulated with respect to the downscaled macroscale quantities $\mathbf{X}$ (Eq. (17)) as an ensemble of the macroscale nodal solutions. While in Eq. (45) the tangent matrices with respect to $\mathbf{U}_\beta$ and $\mathbf{U}_\sigma$ are needed. To this end, we express $\mathbf{X}$ in the matrix form as

$$\mathbf{X} = \begin{bmatrix} \mathbf{BU}_\beta \\ \mathbf{NU}_\beta \\ \mathbf{BU}_\sigma \\ \mathbf{NU}_\sigma \end{bmatrix} \tag{B.11}$$

and thus define

$$\Phi_\beta = \frac{\partial \mathbf{X}}{\partial \mathbf{U}_\beta} = \begin{bmatrix} \mathbf{B} \\ \mathbf{N} \\ \mathbf{0} \\ \mathbf{0} \end{bmatrix} \quad \text{and} \quad \Phi_\sigma = \frac{\partial \mathbf{X}}{\partial \mathbf{U}_\sigma} = \begin{bmatrix} \mathbf{0} \\ \mathbf{0} \\ \mathbf{B} \\ \mathbf{N} \end{bmatrix}. \tag{B.12}$$

The tangent matrices for macroscale fluxes and macroscale sources in Eq. (45) can therefore be computed as

$$\frac{\partial \mathbf{H}_\beta}{\partial \mathbf{U}_\beta} = \mathbf{S}_\beta \Phi_\beta, \frac{\partial \mathbf{H}_\beta}{\partial \mathbf{U}_\sigma} = \mathbf{S}_\beta \Phi_\sigma,$$

$$\frac{\partial \mathbf{H}_\sigma}{\partial \mathbf{U}_\beta} = \mathbf{S}_\sigma \Phi_\beta, \frac{\partial \mathbf{H}_\sigma}{\partial \mathbf{U}_\sigma} = \mathbf{S}_\sigma \Phi_\sigma, \tag{B.13}$$

and

$$\frac{\partial Q_\beta}{\partial \mathbf{U}_\beta} = \mathbf{T}_\beta \Phi_\beta, \quad \frac{\partial Q_\beta}{\partial \mathbf{U}_\sigma} = \mathbf{T}_\beta \Phi_\sigma,$$

$$\frac{\partial Q_\sigma}{\partial \mathbf{U}_\beta} = \mathbf{T}_\sigma \Phi_\beta, \quad \frac{\partial Q_\sigma}{\partial \mathbf{U}_\sigma} = \mathbf{T}_\sigma \Phi_\sigma, \tag{B.14}$$

respectively.

References

[1] M. Quintard, S. Whitaker, One- and two-equation models for transient diffusion processes in two-phase systems, Advances in Heat Transfer 23 (369-465) (1993) 37, doi:10.1016/s0065-2717(08)70009-1.
[2] M. Quintard, M. Kaviany, S. Whitaker, Two-medium treatment of heat transfer in porous media: Numerical results for effective properties, Advances in Water Resources 20 (2-3) (1997) 77–94, doi:10.1016/s0309-1708(96)00024-3.
[3] F. Kuwahara, M. Shirota, A. Nakayama, A numerical study of interfacial convective heat transfer coefficient in two-energy equation model for convection in porous media, International Journal of Heat and Mass Transfer 44 (6) (2001) 1153–1159, doi:10.1016/s0017-9310(00)00166-6.
[4] D.A. Nield, A. Bejan, Convection in Porous Media, Springer New York, 2013, doi:10.1007/978-1-4614-5541-7.
[5] F. Golfier, B.D. Wood, L. Orgogozo, M. Quintard, M. Buès, Biofilms in porous media: Development of macroscopic transport equations via volume averaging with closure for local mass equilibrium conditions, Advances in Water Resources 32 (3) (2009) 463–485, doi:10.1016/j.advwatres.2008.11.012.
[6] L. Orgogozo, F. Golfier, M. Buès, M. Quintard, Upscaling of transport processes in porous media with biofilms in non-equilibrium conditions, Advances in Water Resources 33 (5) (2010) 585–600, doi:10.1016/j.advwatres.2010.03.004.
[7] F.E. Teruel, L. Díaz, Calculation of the interfacial heat transfer coefficient in porous media employing numerical simulations, International Journal of Heat and Mass Transfer 60 (2013) 406–412, doi:10.1016/j.ijheatmasstransfer.2012.12.022.
[8] A. Gandomkar, K. Gray, Local thermal non-equilibrium in porous media with heat conduction, International Journal of Heat and Mass Transfer 124 (2018) 1212–1216, doi:10.1016/j.ijheatmasstransfer.2018.04.011.
[9] S. Whitaker, The Method of Volume Averaging, Springer Netherlands, 1999, doi:10.1007/978-94-017-3389-2.
[10] W. Shyy, S.S. Thakur, H. Ouyang, J. Liu, E. Blosch, Computational Techniques for Complex Transport Phenomena, Cambridge University Press, 1997, doi:10.1017/cbo9780511665462.
[11] B.D. Wood, Technical note: Revisiting the geometric theorems for volume averaging, Advances in Water Resources 62 (2013) 340–352, doi:10.1016/j.advwatres.2013.08.012.
[12] M. Kaviany, Principles of Heat Transfer in Porous Media, Springer New York, 1995, doi:10.1007/978-1-4612-4254-3.
[13] Y. Mahmoudi, N. Karimi, Numerical investigation of heat transfer enhancement in a pipe partially filled with a porous material under local thermal non-equilibrium condition, International Journal of Heat and Mass Transfer 68 (2014) 161–173, doi:10.1016/j.ijheatmasstransfer.2013.09.020.
[14] M. Quintard, S. Whitaker, Local thermal equilibrium for transient heat conduction: Theory and comparison with numerical experiments, International Journal of Heat and Mass Transfer 38 (15) (1995) 2779–2796, doi:10.1016/0017-9310(95)00028-8.
[15] D.A.S. Rees, I. Pop, Local thermal non-equilibrium in porous medium convection, in: Transport Phenomena in Porous Media III, Elsevier, 2005, pp. 147–173, doi:10.1016/b978-008044490-1/50010-7.
[16] A. Gupta, J.H. Seo, X. Zhang, W. Du, A.M. Sastry, W. Shyy, Effective transport properties of LiMn₂O₄ electrode via particle-scale modeling, Journal of The Electrochemical Society 158 (5) (2011) A487–A497, doi:10.1149/1.3560441.
[17] A. Salvadori, E. Bosco, D. Grazioli, A computational homogenization approach for Li-ion battery cells: Part 1 – formulation, Journal of the Mechanics and Physics of Solids 65 (2014) 114–137, doi:10.1016/j.jmps.2013.08.010.
[18] B.D. Wood, F.J. Valdés-Parada, Volume averaging: Local and nonlocal closures using a Green's function approach, Advances in Water Resources 51 (2013) 139–167, doi:10.1016/j.advwatres.2012.06.008.
[19] H. Davarzani, M. Marcoux, M. Quintard, Theoretical predictions of the effective thermodiffusion coefficients in porous media, International Journal of Heat and Mass Transfer 53 (7-8) (2010) 1514–1528, doi:10.1016/j.ijheatmasstransfer.2009.11.044.
[20] R.J.M. Smit, W.A.M. Brekelmans, H.E.H. Meijer, Prediction of the mechanical behavior of nonlinear heterogeneous systems by multi-level finite element modeling, Computer Methods in Applied Mechanics and Engineering 155 (1-2) (1998) 181–192, doi:10.1016/s0045-7825(97)00139-4.
[21] F. Feyel, J.-L. Chaboche, FE² multiscale approach for modelling the elastoviscoplastic behaviour of long fibre SiC/Ti composite materials, Computer Methods in Applied Mechanics and Engineering 183 (3-4) (2000) 309–330, doi:10.1016/s0045-7825(99)00224-8.
[22] V. Kouznetsova, W.A.M. Brekelmans, F.P.T. Baaijens, An approach to micro-macro modeling of heterogeneous materials, Computational Mechanics 27 (1) (2001) 37–48, doi:10.1007/s004660000212.
[23] C. Miehe, Strain-driven homogenization of inelastic microstructures and composites based on an incremental variational formulation, International Journal for Numerical Methods in Engineering 55 (11) (2002) 1285–1322, doi:10.1002/nme.515.
[24] J. Schröder, A numerical two-scale homogenization scheme: the FE² method, in: Plasticity and Beyond, Springer Vienna, 2014, pp. 1–64, doi:10.1007/978-3-7091-1625-8_1.
[25] B.S. Mercer, K.K. Mandadapu, P. Papadopoulos, Novel formulations of microscopic boundary-value problems in continuous multiscale finite element methods, Computer Methods in Applied Mechanics and Engineering 286 (2015) 268–292, doi:10.1016/j.cma.2014.12.021.

[26] T. Qiu, Q. Wang, C. Yang, Upscaling multicomponent transport in porous media with a linear reversible heterogeneous reaction, Chemical Engineering Science 171 (2017) 100–116, doi:10.1016/j.ces.2017.05.018.

[27] I. Özdemir, W.A.M. Brekelmans, M.G.D. Geers, Computational homogenization for heat conduction in heterogeneous solids, International Journal for Numerical Methods in Engineering 73 (2) (2007) 185–204, doi:10.1002/nme.2068.

[28] I. Özdemir, W. Brekelmans, M. Geers, FE^2 computational homogenization for the thermo-mechanical analysis of heterogeneous solids, Computer Methods in Applied Mechanics and Engineering 198 (3-4) (2008) 602–613, doi:10.1016/j.cma.2008.09.008.

[29] F. Larsson, K. Runesson, F. Su, Variationally consistent computational homogenization of transient heat flow, International Journal for Numerical Methods in Engineering 81 (13) (2010) 1659–1686, doi:10.1002/nme.2747.

[30] A. Sengupta, P. Papadopoulos, R.L. Taylor, A multiscale finite element method for modeling fully coupled thermomechanical problems in solids, International Journal for Numerical Methods in Engineering 91 (13) (2012) 1386–1405, doi:10.1002/nme.4320.

[31] G.R. Ramos, T. dos Santos, R. Rossi, An extension of the Hill-Mandel principle for transient heat conduction in heterogeneous media with heat generation incorporating finite RVE thermal inertia effects, International Journal for Numerical Methods in Engineering 111 (6) (2017) 553–580, doi:10.1002/nme.5471.

[32] G.R. Ramos, R. Rossi, A novel computational multiscale approach to model thermochemical coupled problems in heterogeneous solids: Application to the determination of the "state of cure" in filled elastomers, Computer Methods in Applied Mechanics and Engineering 351 (2019) 694–717, doi:10.1016/j.cma.2019.03.055.

[33] A. Waseem, T. Heuzé, L. Stainier, M.G.D. Geers, V.G. Kouznetsova, Model reduction in computational homogenization for transient heat conduction, Computational Mechanics 65 (1) (2019) 249–266, doi:10.1007/s00466-019-01767-3.

[34] A. Waseem, T. Heuzé, L. Stainier, M.G.D. Geers, V.G. Kouznetsova, Enriched continuum for multi-scale transient diffusion coupled to mechanics, Advanced Modeling and Simulation in Engineering Sciences 7 (1) (2020), doi:10.1186/s40323-020-00149-2.

[35] A. Waseem, T. Heuzé, L. Stainier, M. Geers, V. Kouznetsova, Two-scale analysis of transient diffusion problems through a homogenized enriched continuum, European Journal of Mechanics - A/Solids 87 (2021) 104212, doi:10.1016/j.euromechsol.2021.104212.

[36] E. Aggestam, F. Larsson, K. Runesson, F. Ekre, Numerical model reduction with error control in computational homogenization of transient heat flow, Computer Methods in Applied Mechanics and Engineering 326 (2017) 193–222, doi:10.1016/j.cma.2017.08.006.

[37] M. Geers, V. Kouznetsova, W. Brekelmans, Multi-scale computational homogenization: Trends and challenges, Journal of Computational and Applied Mathematics 234 (7) (2010) 2175–2182, doi:10.1016/j.cam.2009.08.077.

[38] R. Hill, Elastic properties of reinforced solids: Some theoretical principles, Journal of the Mechanics and Physics of Solids 11 (5) (1963) 357–372, doi:10.1016/0022-5096(63)90036-x.

[39] J. Schröder, Derivation of the localization and homogenization conditions for electro-mechanically coupled problems, Computational Materials Science 46 (3) (2009) 595–599, doi:10.1016/j.commatsci.2009.03.035.

[40] D. Perić, E.A. de Souza Neto, R.A. Feijóo, M. Partovi, A.J.C. Molina, On micro-to-macro transitions for multi-scale analysis of non-linear heterogeneous materials: Unified variational basis and finite element implementation, International Journal for Numerical Methods in Engineering 87 (1-5) (2010) 149–170, doi:10.1002/nme.3014.

[41] E. de Souza Neto, P. Blanco, P. Sánchez, R. Feijóo, An RVE-based multiscale theory of solids with micro-scale inertia and body force effects, Mechanics of Materials 80 (2015) 136–144, doi:10.1016/j.mechmat.2014.10.007.

[42] C. Miehe, J. Dettmar, A framework for micro–macro transitions in periodic particle aggregates of granular materials, Computer Methods in Applied Mechanics and Engineering 193 (3-5) (2004) 225–256, doi:10.1016/j.cma.2003.10.004.

[43] O.C. Zienkiewicz, R.L. Taylor, J.Z. Zhu, The finite element method: Its basis and fundamentals, Elsevier, 2005.

[44] A.F. Bower, Applied Mechanics of Solids, CRC Press, 2009, doi:10.1201/9781439802489.

[45] S. Fernández-Méndez, A. Huerta, Imposing essential boundary conditions in mesh-free methods, Computer Methods in Applied Mechanics and Engineering 193 (12-14) (2004) 1257–1275, doi:10.1016/j.cma.2003.12.019.

[46] M. Quintard, L. Bletzacker, D. Chenu, S. Whitaker, Nonlinear, multicomponent, mass transport in porous media, Chemical Engineering Science 61 (8) (2006) 2643–2669, doi:10.1016/j.ces.2005.11.034.

[47] J. Hager, S. Whitaker, Transport in Porous Media 46 (1) (2002) 19–35, doi:10.1023/a:1013801627353.